




Article

Improvement of Marine Steam Turbine Conventional Exergy Analysis by Neural Network Application

Sandi Baressi Šegota ¹, Ivan Lorencin ¹, Nikola Anđelić ¹ , Vedran Mrzljak ^{2,*} 
and Zlatan Car ¹ 

¹ Department of Automation and Electronics, Faculty of Engineering, University of Rijeka, Vukovarska 58, 51000 Rijeka, Croatia; sbaressisegota@riteh.hr (S.B.Š.); ilorencin@riteh.hr (I.L.); nandelic@riteh.hr (N.A.); car@riteh.hr (Z.C.)

² Department of Thermodynamics and Energy Engineering, Faculty of Engineering, University of Rijeka, Vukovarska 58, 51000 Rijeka, Croatia

* Correspondence: vmrzljak@riteh.hr; Tel.: +385-51-651-551

Received: 13 October 2020; Accepted: 3 November 2020; Published: 5 November 2020



Abstract: This article presented an improvement of marine steam turbine conventional exergy analysis by application of neural networks. The conventional exergy analysis requires numerous measurements in seven different turbine operating points at each load, while the intention of MLP (Multilayer Perceptron) neural network-based analysis was to investigate the possibilities for measurements reducing. At the same time, the accuracy and precision of the obtained results should be maintained. In MLP analysis, six separate models are trained. Due to a low number of instances within the data set, a 10-fold cross-validation algorithm is performed. The stated goal is achieved and the best solution suggests that MLP application enables reducing of measurements to only three turbine operating points. In the best solution, MLP model errors falling within the desired error ranges (Mean Relative Error) $MRE < 2.0\%$ and (Coefficient of Correlation) $R^2 > 0.95$ for the whole turbine and each of its cylinders.

Keywords: exergy destruction; exergy efficiency; marine steam turbine; MLP neural network; turbine cylinders

1. Introduction

The dominant usage of steam turbines worldwide is related to electrical generator drive and electricity production [1,2]. Steam power plants, with steam turbines as essential components, can be assembled by following various methodologies. Along with conventional steam power plants [3] and nuclear power plants [4,5], the novel approach in steam power plant design is the usage of various renewable energy sources which can notably improve steam power plant operation and its efficiency, and which are very beneficial to the environment [6,7]. The reduction of harmful emissions from such plants is today one of the most important research and scientific topic and multiple researchers are developing various techniques and processes with a goal of emissions reduction [8–10].

In addition to being used as stand-alone systems, steam power plants can be integrated into more complex systems, such as combined cycle power plants [11]. In combined cycle power plants, waste heat from the gas turbine is used for superheated steam production—in such a way, the environment is protected from huge waste heat amount and the reduction in harmful emissions (in comparison to pure gas or pure steam power plants) is also notable [12,13]. Such an operation of combined cycle power plants results in high efficiency, much higher in comparison to the conventional or nuclear steam power plants [14,15].

In marine power systems, internal combustion engines take a dominant share in the entire world fleet [16]. Due to internal combustion engine dominance, various researchers are involved in investigating improvements as well as in minimizing the overall harmful impact on the environment [17–19]. Steam power plants are generally rarely used in marine power systems. However, there are several marine engineering fields in which steam power plants are still dominant. Additionally, steam power plants can be found as a part of new, complex marine systems that are currently under development [20,21]. All aforementioned benefits of combined cycle power plants are also present in the marine power systems [22,23]. The complexity of combined cycle power plants, especially for marine usage, requires adequate control and regulation systems for its proper (or if possible, optimal) operation.

One of the marine fields in which steam power plants are still predominantly used is the propulsion of LNG (Liquefied Natural Gas) carriers, but it should be noted that the utilization share of internal combustion engines, especially dual-fuel engines, is also increasing [24,25]. There are several steam turbines in the steam propulsion plant of any steam-powered LNG carrier. Along with the main turbine used for the propulsion propeller (or several propellers) drive, in such plants two or more steam turbines are mounted for the electrical generators drive (turbo-generators) [26,27] and low power steam turbine for the main feed water pump drive [28].

Analysis of any component from the steam power plant can be performed by using various approaches and techniques presented in the literature [29,30]. For the analysis of the main marine steam turbine observed in this research, exergy analysis is used. Exergy analysis of any component or the entire system is a technique that offers many benefits in comparison to other analysis methods. Exergy analysis does not take into consideration processes that occur inside any component—for the exergy analysis, only fluid flows and heat transfer (to and from the analyzed component) as well as used or produced mechanical power are necessary. Therefore, for the exergy analysis, details about the analyzed component's inner structure are not required, simplifying all necessary measurements [31,32]. On the other hand, a lack of information about the inner structure of the observed component does not allow research and analysis of many details and processes inside the component. All the exergy analysis benefits can be seen in a variety of scientific papers that take this analysis as the baseline.

If considering the analyses of the entire power plants, Ahmadi and Toghraie [33] applied exergy analysis for the investigation of Montazeri steam power plant in Iran, while Si et al. [34] used the same analysis for the investigation of a 1000 MW double reheat ultra-supercritical power plant. Ibrahim et al. [35] analyzed the thermal performance of the gas turbine power plant, while Aghbashlo et al. [36] observed the performance assessment of a wind power plant by using exergy analysis. AlZahrani and Dincer, I. [37] observed parabolic trough solar power plant and Abuelnuor et al. [38] investigated Garri "2" combined cycle power plant also by using exergy analysis.

Exergy analysis is successfully applied in the performance analysis of many components and processes from various plants. Zhao et al. [39] used exergy analysis for the investigation of the turbine system in a 1000 MW double reheat ultra-supercritical power plant. Medica-Viola et al. [40] used exergy analysis for the performance analysis of low-power steam turbine with one extraction used in marine applications. Presciutti et al. [41] applied exergy analysis for the investigation of glycerol combustion in an innovative flameless power plant. Szablowski et al. [42] used exergy analysis for the investigation of an adiabatic compressed air energy storage system. Arshad et al. [43] performed a review of the exergy analysis usage in the investigation of fuel cells. Lorencin et al. [44] applied exergy analysis for the analysis of steam mass flow rate leakage through steam turbine labyrinth (gland) seals.

Exergy analysis can also be a baseline for the economic analysis of various power plants or its components [45–47]. From the literature, it can be found that exergy analysis is used in the investigation and observation of many other plants, processes and components.

Along with exergy analysis, an extensive literature review also shows that many scientists and researchers used various artificial intelligence methods and processes in the analysis of power plants or its components.

One of the most used artificial intelligence methods in the energy sector is MLP (Multilayer Perceptron) neural network. Sun et al. [48] developed a new MLP-based soft sensor for SO₂ power plant emissions detection. Several researchers [49–52] used MLP for predicting electrical power output from various complex power plants. Wahid et al. [53] applied MLP for the prediction of energy consumption in the buildings. Tahan et al. [54] used MLP for condition-based maintenance of gas turbine, while Lorencin et al. [55] also used MLP for condition-based maintenance, but not for the gas turbine only, then for the entire marine CODLAG (Combined Diesel and Gas) propulsion system. Many other authors also used MLP for the condition-based maintenance problems of various plants and components [56,57].

MLP can also be used for predicting ship speed by using some of the ship propulsion system parameters [58]. Detecting and diagnosing faults by applying MLP in a steam turbine that operates in a thermal power plant was presented Dhini et al. [59], while Tian et al. [60] and Ayo-Imoru and Cilliers [61] used MLP for detecting various losses and prevention of accidents in the nuclear power plants. Various other neural network applications can also be found in the literature in many energy sectors and processes [62–64].

An extensive literature review shows that MLP is not used currently for tracking operating parameters or performances of the main marine steam turbine and all its cylinders. Additionally, the possibility that measurements are reduced by MLP neural network application is not investigated. During the possible reduction of measurements, the dominant goal for MLP must be high accuracy and precision in the prediction of any required operating parameter. The intention of this paper is not only to fill the literature gap but also to show possibilities that neural network applications offer in marine systems (or its components) and to be a guideline for other researchers interested in this field.

In the presented paper, exergy analysis of the main marine steam turbine (as well as both of its cylinders) is performed. The analysis is based on the measurement data obtained during steam turbine exploitation at 24 different loads. At the beginning, the conventional exergy analysis is performed, which requires many measurements at each turbine load. After conventional analysis, an exergy analysis is performed by the MLP neural network application. The application of MLP can significantly reduce the amount of performed measurements, while the accuracy and precision of the obtained exergy analysis parameters remain high, regardless of the observed load. This analysis can be a guideline for reducing control and measurement equipment inside the marine steam power plant, especially on new ships.

2. Description and Operation Principle of the Analyzed Main Marine Steam Turbine

The main marine steam turbine analyzed in this paper operates at the 100,450 tons (gross tonnage) commercial LNG carrier. A steam turbine is used for the LNG carrier propulsion. The maximum mechanical power that can be produced by the observed turbine is 29,420 kW, according to the manufacturer specifications [65]. The general scheme of the analyzed turbine, along with operating points required for the exergy analysis, is presented in Figure 1.

The main marine steam turbine is composed of two cylinders and these are High Pressure Cylinder (HPC) and Low Pressure Cylinder (LPC). Each marine steam propulsion system consists of two parallel operating steam generators which produce superheated steam and delivers the majority of cumulatively produced steam mass flow rate (it depends on the system load) to the HPC inlet [66]. HPC has one steam extraction used for steam delivery to various auxiliary steam plant processes—HFO (Heavy Fuel Oil) heater, BOG (Boil Off Gas) heater, water heater for the crew requirements, etc. Both steam generators in this marine steam plant simultaneously use HFO and BOG during operation. After extraction, the remaining steam mass flow rate expands through HPC until the cylinder outlet. HPC consists of one Curtis and seven Rateau stages.

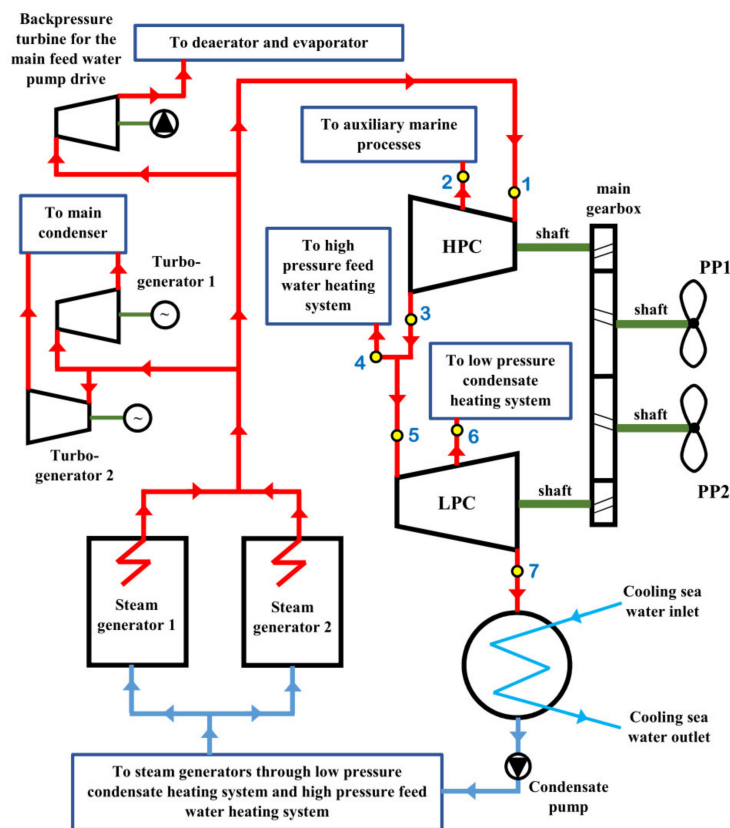


Figure 1. Scheme of the main marine steam turbine along with operating points required for the exergy analysis. HPC: High Pressure Cylinder; LPC: Low Pressure Cylinder; PP1: The first Propulsion Propeller; PP2: The second Propulsion Propeller.

The analyzed main steam turbine is an older variant of marine propulsion steam turbines and it is designed without steam reheating. Newer variants of marine propulsion steam turbines have one additional cylinder, Intermediate Pressure Cylinder (IPC), and steam reheating (steam reheaters are mounted inside steam generators) [67,68]. Such an upgrade increases plant overall efficiency, but simultaneously increases plant complexity and requires more stringent maintenance in comparison to older marine propulsion steam turbines.

Between the HPC and LPC of the analyzed turbine, one additional extraction is mounted for steam delivery to a high pressure feed water heating system. In the observed commercial LNG carrier, the high pressure feed water heating system consists of one high pressure feed water heater and deaerator [69]. In some operating regimes, when required, a part of steam extracted in this extraction (operating point 4, Figure 1), is delivered to air heaters used for heating of air at the steam generators entrance.

The remaining steam mass flow rate (operating point 5, Figure 1) expands through LPC. LPC, similar to HPC, has one steam extraction which is used for steam delivery to low pressure condensate heating system, which in the observed plant consists of one low pressure condensate heater and evaporator. An evaporator is a component used for the freshwater production (from sea water) and simultaneously for condensate heating [70]. After expansion in LPC, the remaining steam mass flow rate is delivered to the main marine steam condenser for condensation [71]. LPC consists of eight Rateau stages.

All three steam extractions from the observed turbine are not open all the time during the main turbine operation. Regulation valves opened and closed each of these extractions (and regulate extracted steam mass flow rate in each extraction) according to the predefined regulation procedure (following operation dynamic of the whole plant).

Both cylinders of the observed turbine are connected to the main marine gearbox through which one or two propulsion propellers are driven (in Figure 1 are shown two propulsion propellers, PP1 and PP2) [72].

It should be noted that in this exergy analysis (both conventional and with MLP application) several additional losses that occur in the plant, related to the main steam turbine, are neglected. For example, these losses are steam mass flow rate leakage through gland seals of each cylinder [73], heat losses in the pipelines and through the housing of each cylinder, mechanical losses [74], etc. Although important, all of these losses have a minor impact on the exergy analysis results of the observed steam turbine and each turbine cylinder.

3. Conventional Exergy Analysis of Main Marine Steam Turbine and Each of its Cylinders

Conventional exergy analysis of the main marine steam turbine and its cylinders is characterized by the fact that three steam operating parameters (steam temperature, pressure and mass flow rate) must be measured in each operating point presented in Figure 1 at each turbine load. Thus, each turbine load requires 21 measured data in order to be able to perform conventional exergy analysis at that particular load for the whole turbine and each cylinder. Change in turbine load requires new three measured data in each operating point. Therefore, conventional exergy analysis of observed main marine steam turbine and its cylinders require extensive measurements at each turbine load. Without these measurements (if any steam operating parameter, in any operating point from Figure 1 is missing), proper conventional exergy analysis cannot be performed or certain approximations must be used.

3.1. Overall Exergy Analysis Balances and Equations

In comparison to the energy analysis, of which results are not dependable on the ambient conditions [75,76], exergy analysis of any control volume or a system is dependable on the ambient conditions (ambient temperature and pressure) [77,78]. For the proper conventional exergy analysis of any control volume or a system, an overall exergy balance, mass flow rate balance and the most important variables should be defined. These overall equations and balances are valid in any exergy analysis, as well as in exergy analysis of the observed main marine steam turbine and both of its cylinders [79].

The overall steady-state exergy balance equation is defined as recommended in [80] by using an Equation (1):

$$\dot{Q}_{EX} + P_{INLET} + \sum \dot{E}x_{INLET} = P_{OUTLET} + \sum \dot{E}x_{OUTLET} + \dot{E}x_{DES}. \quad (1)$$

where P is the mechanical power (used or produced) and $\dot{E}x_{DES}$ is exergy destruction (exergy loss). It should be highlighted that in the overall exergy balance equation, potential and kinetic energies are disregarded due to its low influence on the overall balance. For the analyzed main marine steam turbine and its cylinders potential and kinetic energies in above balance are also low, and their inclusion will not bring meaningful change in the obtained results [81]. \dot{Q}_{EX} is the exergy transfer by heat at the temperature T , of which the definition can be found in the literature [82] through the following Equation (2):

$$\dot{Q}_{EX} = \sum \left(1 - \frac{T_0}{T}\right) \dot{Q}, \quad (2)$$

where \dot{Q} is an energy transfer by heat, T is temperature and index 0 corresponds to the state of the ambient. The last undefined variable from the overall exergy balance equation is a total exergy power of operating medium flow ($\dot{E}x$), of which definition can be found in [83], Equation (3):

$$\dot{E}x = \dot{m} \cdot \varepsilon. \quad (3)$$

where \dot{m} is operating medium mass flow rate and ε is specific flow exergy of operating medium. Operating medium specific flow exergy is calculated according to the Equation (4), [84]:

$$\varepsilon = (h - h_0) - T_0 \cdot (s - s_0), \quad (4)$$

where h is operating medium specific enthalpy and s is operating medium specific entropy. During control volume or a system standard operation, mass flow rate leakage did not occur. By taking into account the fact that for the analyzed main marine steam turbine and its cylinders all the standard small steam leakages (as for example, leakage through gland seals of each cylinder) are neglected as described above, the valid mass flow rate balance is [85], Equation (5):

$$\sum \dot{m}_{\text{INLET}} = \sum \dot{m}_{\text{OUTLET}}. \quad (5)$$

The overall definition of the exergy efficiency can be presented as proposed in [86], Equation (6):

$$\eta_{\text{EX}} = \frac{\text{CUMULATIVE EXERGY OUTLET}}{\text{CUMULATIVE EXERGY INLET}}, \quad (6)$$

with the note that exergy efficiency of any observed control volume or a system can significantly differ from the overall definition, which depends on operating characteristics and operation principles of each control volume or a system.

3.2. Equations for the Exergy Analysis of Main Marine Steam Turbine and Its Cylinders

For each cylinder and the whole turbine, the first step is the calculation of the developed mechanical power. This step represents the essential element in exergy analysis equations. After developing the mechanical power equations, equations for the calculation of exergy destruction and exergy efficiency will be presented for each cylinder and the whole turbine. All the equations are defined according to recommendations from the literature [87,88] and are related to operating points presented in Figure 1.

3.2.1. High Pressure Cylinder (HPC)

Developed mechanical power, Equation (7):

$$P_{\text{HPC}} = \dot{m}_1 \cdot (h_1 - h_2) + (\dot{m}_1 - \dot{m}_2) \cdot (h_2 - h_3). \quad (7)$$

Exergy destruction (exergy loss), Equation (8):

$$\dot{E}x_{\text{DES,HPC}} = \dot{E}x_1 - \dot{E}x_2 - \dot{E}x_3 - P_{\text{HPC}}. \quad (8)$$

Exergy efficiency, Equation (9):

$$\eta_{\text{EX,HPC}} = \frac{P_{\text{HPC}}}{\dot{E}x_1 - \dot{E}x_2 - \dot{E}x_3}. \quad (9)$$

3.2.2. Low Pressure Cylinder (LPC)

Developed mechanical power, Equation (10):

$$P_{\text{LPC}} = \dot{m}_5 \cdot (h_5 - h_6) + (\dot{m}_5 - \dot{m}_6) \cdot (h_6 - h_7). \quad (10)$$

Exergy destruction (exergy loss), Equation (11):

$$\dot{E}x_{\text{DES,LPC}} = \dot{E}x_5 - \dot{E}x_6 - \dot{E}x_7 - P_{\text{LPC}}. \quad (11)$$

Exergy efficiency, Equation (12):

$$\eta_{EX,LPC} = \frac{P_{LPC}}{\dot{E}x_5 - \dot{E}x_6 - \dot{E}x_7}. \quad (12)$$

3.2.3. Whole Turbine (WT)

Developed mechanical power, Equation (13):

$$P_{WT} = P_{HPC} + P_{LPC}. \quad (13)$$

Exergy destruction (exergy loss), Equation (14):

$$\dot{E}x_{DES,WT} = \dot{E}x_1 - \dot{E}x_2 - \dot{E}x_4 - \dot{E}x_6 - \dot{E}x_7 - P_{WT}. \quad (14)$$

Exergy efficiency, Equation (15):

$$\eta_{EX,WT} = \frac{P_{WT}}{\dot{E}x_1 - \dot{E}x_2 - \dot{E}x_4 - \dot{E}x_6 - \dot{E}x_7}. \quad (15)$$

In the equations for the exergy destruction and exergy efficiency of the whole turbine and each cylinder, total exergy power of steam flow ($\dot{E}x$) and steam specific flow exergy (ε) should be calculated using Equations (3) and (4) in each operating point from Figure 1. Additionally, the overall exergy balance equation, Equation (1), and steam mass flow rate balance, Equation (5), should always be satisfied for each cylinder and the whole turbine at each load.

4. Exergy Analysis of Main Marine Steam Turbine and Each of its Cylinders by MLP Neural Network Application

MLP is a neural network that consists of artificial neurons arranged into multiple layers. MLP consists of at least three layers—an input layer, output layer and one or more hidden layers [89,90]. Neurons in input layers are used to set inputs for the MLP model. The number of neurons in that layer is equal to the number of inputs of the data set, and their values are set to the number of input values contained within the data set [89,91]. The subsequent layers consist of neurons whose values are calculated depending on inputs and connection weights—with each artificial neuron in the subsequent layer being connected to all the artificial neurons in the preceding neurons with weighted connections [92,93]. If it is assumed that the value of the neuron is y_i^k , where k represents the layer number and i the neuron number within the layer, then the value of that particular artificial neuron is calculated as the activated weighted sum of artificial neurons of the previous layer [89], Equation (16):

$$y_i^k = F \left(\sum_{j=0}^{n_k} \theta_{j,i}^{k-1} \cdot y_j^{k-1} \right), \quad (16)$$

where $\theta_{j,i}^{k-1}$ represents the weight of the connection between the artificial neuron j in layer $k-1$ (y_j^{k-1}) and the artificial neuron i in the layer k (y_i^k). F represents the activation function—the function used to map the value of neuron into the desired range of values. Commonly used activation functions may [94,95]:

- Eliminate the unwanted values such as Rectified linear unit—ReLU ($y = \max(0, x)$)—used to eliminate negative values [95],
- Map the input files to a certain range such as sigmoid (logistic) function which maps the values to a range of $[0, 1]$ ($y = \frac{1}{1+e^{-x}}$) or hyperbolic tangent function which maps them to the range of $[-1, 1]$ ($y = \tanh(x)$),

- Simply map the input directly to output as is the case with the identity activation function ($y = x$) [96,97].

As MLP belongs to the family of machine learning algorithms, it has the ability to adjust itself to the data used for training it. This is done through the process of training, divided into forward and backward propagation [89,98]. In the forward propagation part of the training process, a single set of the input data values (steam temperature, pressure and mass flow rate in used operating points, Figure 1, along with the ambient pressure and temperature) are used as input neuron values (where the number of input neurons equals the total number of inputs). Then, weights of inter-neuron connections are set randomly and the values of neurons in the hidden layer. Finally, the output layer values are calculated using Equation (16) [89,92]. The output value is compared to the value of one of the outputs—either exergy destruction (exergy loss) or exergy efficiency—and the general output contained within the dataset is marked with y . It can be expected that the MLP output, marked \hat{y} , will have a certain error $\epsilon = \sqrt{(y - \hat{y})^2}$. This error is then used in the backward propagation process in order to adjust the weights based on the gradient of the error (with a higher error values causing a larger adjustment being made to the weights). If the vector of the weights in a layer k is marked as $\Theta^k = [\theta_1^k \theta_2^k \dots \theta_{n_k}^k]$, and learning rate with α , this can be written as [58,89], Equation (17):

$$\Theta_{new}^k = \Theta_{old}^k - \alpha \frac{\partial \epsilon}{\partial \Theta_{old}^k}. \quad (17)$$

By repeating the described training process for multiple sets of input and output values, the MLP weights can be finely adjusted and provide a very low error when used as a trained model. The dataset consists of 125 points, each of which has data entries for the ambient temperature and pressure, as well as steam mass flow rate, temperature and pressure in each of the seven operating points (Figure 1), as well as values of exergy destruction and exergy efficiency for high pressure cylinder, low pressure cylinder and the whole turbine. This means that each data point has 23 input values and 6 output values. It should be noted that by its nature, MLP can only regress a single value within a model, and the number of inputs need to be fixed. Due to this fact, each output and each separate input set need to have a separate model trained.

Each of the listed input combinations will have two models trained—one for each of the possible outputs—exergy destruction and exergy efficiency. Due to this, the total number of final models is 72. Each of the models trained will need to have hyperparameters adjusted to achieve a quality regression performance. Hyperparameters are values which describe the general architecture of the neural network used to train the model. Hyperparameters of the MLP need to be varied to achieve the best regression models for each case. One of the varied hyperparameters is the earlier described activation function of the hidden layer neurons [96]. Further hyperparameters include the number of hidden layers and the number of neurons per hidden layer expressed as (k_1, k_2, \dots, k_n) in which the total number of layers is n and k_i represents the number of neurons in layer i . The algorithm used for calculating the weight values during the training process, called a solver, is also one of the varied hyperparameters [99]. Additional varied hyperparameters are the learning rate, which adjusts the rate of the weight adjustment during the backpropagation process, as well as the type of the learning rate—whether its value will remain constant or scale depending on the number of iterations [100]. Finally, hyperparameter is the L2 regularization parameter, which, if high, penalizes the inputs which have a high individual influence on the MLP output value—which can result in underfitted models [101].

In order to find the optimal set of hyperparameters, the Grid Search (GS) algorithm can be used. GS works in a way that it calculates all possible hyperparameter combinations. Then, a neural network is trained with each of this hyperparameter combinations [102]. In this manner, a wide range of hyperparameters can be tested. While the algorithm might not find the best possible combination of hyperparameters, with enough hyperparameters, it can find a hyperparameter combination which is

close to the best one [103]. If needed, for example, if none of the yielded models provide satisfactory performance, possible hyperparameter values can be expanded or further refined, around the hyperparameter combination that provides the best results [58,104].

Finally, the metrics that will define the quality of the model solution need to be defined. In machine learning algorithms, models are evaluated by splitting the data set into training and testing portions [89,98]. The training portion is used during the previously described training process, and the trained model is evaluated on the testing portion. This is done by performing solely the forward propagation of the training process in order to obtain pairs of predicted values (\hat{y}_i) which can then be compared to the real values (y) from the data set. This will provide the value that describes the performance of the model. Two such metrics are used in this paper and those are coefficient of correlation (R^2) and mean absolute error (MAE).

R^2 defines the ratio of variance which exists inside the data set with the amount of variance contained in the results of the trained models [105]. Less unexplained variance means that the model is tracking the real data better, with higher values of R^2 , which is defined in the range from 0 to 1 [106]. R^2 is defined by the Equation (18), [105]:

$$R^2 = 1 - \frac{S_{RESIDUAL}}{S_{TOTAL}} = 1 - \frac{\sum_{i=1}^n (y_i - \hat{y})^2}{\sum_{i=1}^n (y_i - \frac{1}{n} \sum_{i=1}^n y_i)^2}. \quad (18)$$

MAE provides a clearer, direct value of the error which using the MLP model introduces when used for regression [107]. MAE is defined as [107,108], Equation (19):

$$MAE = \frac{1}{n} \sum_{i=1}^n |y_i - \hat{y}_i|. \quad (19)$$

As the data set used in this research is relatively small, the need for cross-validation arises. Cross-validation is a technique which allows a larger amount of data to be used for testing. As the splits of training and testing data are randomized, a situation can happen in which a bad model performs well on a randomized testing set—while its real performance on the entire dataset is comparatively low [50,109,110]. A K-fold cross-validation, with 10 folds, is performed. This technique is applied in the following manner: first, the data set is split into K splits. Then, the model with the architecture provided from the grid search is trained on the training set consisting of the mix of $K - 1$ subsets, with the remaining 1 being used as the testing set [92,111]. This process is performed K times, with no repetitions of testing splits—in other words, until all the splits have been used as the testing split exactly once. In this manner, the entire dataset is used as the testing set, providing more detailed information on the model performance. In the case of the 10-fold K-fold cross-validation, each split is trained with 90% of the dataset (9 folds) used as the training set, and 10% used as the testing set (1 fold). The metrics defined with the Equations (18) and (19) are applied on all K training/testing set combinations, and the final scoring is expressed as the average score over the K fold, along with the standard error of that value. To summarize, for each of the 72 input/output combinations, 6144 different MLP model architectures are trained for 10 cross-validation folds, and evaluated using R^2 and MAE metrics across all folds. This provides the average and standard error values which allow the models for each parameter combination to be compared and the best achieved model hyperparameter values to be determined. This process is illustrated in Figure 2.

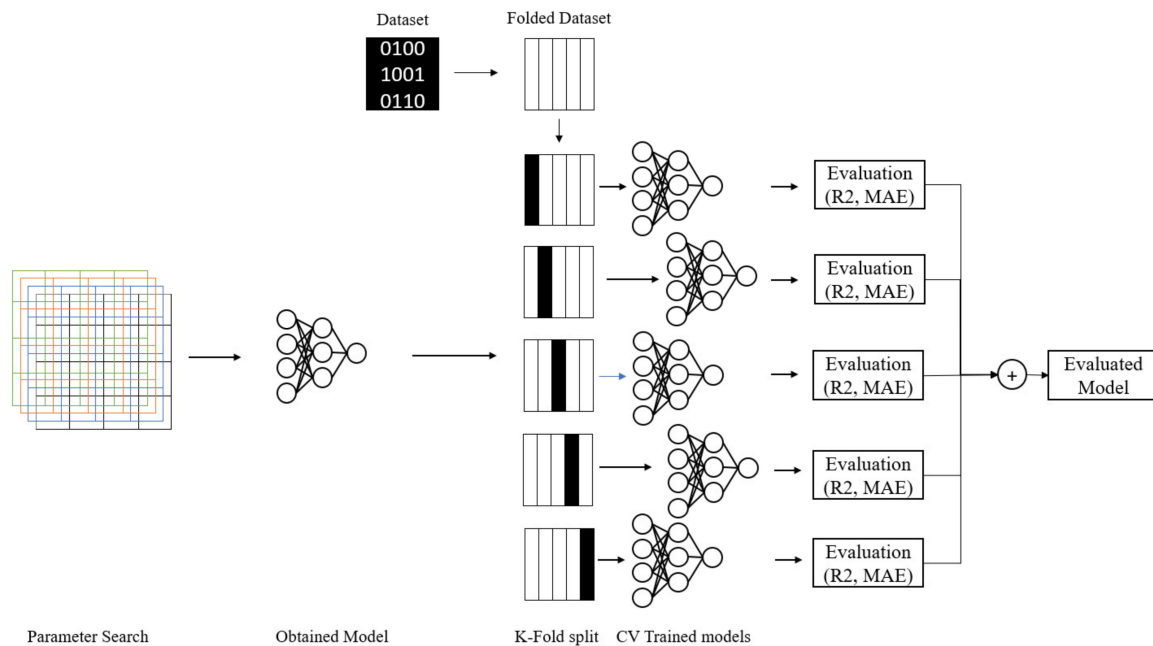


Figure 2. The illustration of the Multilayer Perceptron (MLP) process used in the research, starting with the parameter search performed using a grid search (GS), yielding the MLP model, which is then applied on separate K-Fold splits and evaluated using R^2 and MAE metrics.

The implementation of the described algorithm is done in the Python programming language, using Scikit-Learn machine learning library. Scikit-Learn was chosen for this research because it implements all the necessary algorithms for the presented research. Namely, the described Multilayer Perceptron, as used for a regression problem, is implemented within the MLPRegressor function, which takes the hyperparameters as the input [99]. Grid Search and K-Fold cross validation were implemented using the GridSearchCV function, which takes the number of folds (10), the selected algorithm (MLPRegressor), possible hyperparameter values stored within a dictionary data structure (with the names of hyperparameters being used as keys) and the list of desired metrics as inputs [99,100]. Helpfully, the metrics used are also implemented within Scikit-Learn, or to be more precise, within the metrics module as mean absolute error and R^2 ; both of which take the least actual dataset values and a list of predicted values as inputs [99,101].

The training of the models was performed using University of Rijeka's Bura supercomputer. Models for each output and input combination were trained on a single node, so a total of 72 nodes were used. Each node of the Bura supercomputer consists of an Intel Xeon E5 CPU, which provides 24 physical or 48 logical cores, and 64 GB of RAM. At the time of the research Bura supercomputer used Red Hat Enterprise Linux operating system, with kernel version 3.10.0-957 [112]. Use of Scikit-Learn was enabled through Anaconda Data Science platform, version 4.8.4. [113].

5. Steam Operating Parameters Required for the Exergy Analysis

For the purpose of conventional exergy analysis and exergy analysis by MLP neural network application of the main marine steam turbine and both its cylinders, in this research measurements are performed in each operating point from Figure 1 at 24 different turbine loads. Turbine load will be presented in relation to maximum turbine power (29,420 kW) specified by the turbine manufacturer. The maximum measured load equals to 84.31% of maximum power, which corresponds with minimum specific fuel consumption of the steam propulsion plant. Measurements on the LNG carrier were obtained at 24 steady-state conditions. It should be highlighted that the authors did not have any permission to get involved in the ship operation or to influence the ship crew.

The conventional exergy analysis the complete data will be presented in three turbine loads—low, medium, and high load, which correspond to 7.03%, 49.79% and 83.22% of the maximum turbine power, respectively.

For the turbine exergy analysis by MLP neural network application, all the collected data are used at all measured turbine loads. Those data will not be fully presented, for each measured steam operating parameter in each point from Figure 1 will be presented data range (from minimum to maximum) collected in all 24 turbine loads.

5.1. Conventional Exergy Analysis

Steam operating parameters in each operating point from Figure 1 at three different loads, required for the conventional exergy analysis of the main marine steam turbine and its cylinders are presented in Tables 1–3. In Table 1 steam data are presented for low turbine load, which corresponds to 7.03% of turbine maximum power, in Table 2 data are presented for medium turbine load (49.79% of maximum turbine power) and in Table 3 data are presented for high turbine load (83.22% of turbine maximum power).

Table 1. Steam operating parameters at low load (7.03% of maximum power).

Operating Point *	Temperature (°C)	Pressure (MPa)	Mass Flow Rate (kg/h)
1	487	6.2	9622
2	-	-	0
3	235	0.097	9622
4	-	-	0
5	235	0.097	9622
6	-	-	0
7	62.13	0.00511	9622

* Operating point numeration refers to Figure 1.

Table 2. Steam operating parameters at medium load (49.79% of maximum power).

Operating Point *	Temperature (°C)	Pressure (MPa)	Mass Flow Rate (kg/h)
1	511	6.065	51,419
2	-	-	0
3	259	0.401	51,419
4	-	-	0
5	259	0.401	51,419
6	158	0.085	2985
7	28.85	0.00397	48,434

* Operating point numeration refers to Figure 1.

Table 3. Steam operating parameters at high load (83.22% of maximum power).

Operating Point *	Temperature (°C)	Pressure (MPa)	Mass Flow Rate (kg/h)
1	500	5.795	95,570
2	354	1.558	3398
3	250	0.590	92,172
4	250	0.590	13,172
5	250	0.590	79,000
6	154	0.120	4636
7	34.80	0.00557	74,364

* Operating point numeration refers to Figure 1.

Steam-specific enthalpy and specific entropy in each operating point at all loads are calculated from the measured steam temperature and pressure by using NIST-REFPROP 9.0 software [114]. Steam-specific flow exergy in each operating point for all turbine loads is calculated by using

Equation (4). The steam specific flow exergy calculation requires definition of the ambient state in which analyzed steam turbine operates—in this research, the ambient state is defined as proposed in the literature [115] through the ambient temperature of 25 °C and the ambient pressure of 1 bar.

By observing data from Tables 1–3, operation dynamics of the analyzed steam turbine can be seen during its load variations. At low turbine load (Table 1) all three steam extractions are closed—an increase in turbine load results in steam extractions opening, due to an increase in the steam mass flow rate delivered to the main turbine. The third and last steam extraction (operating point 6, Figure 1) is the first which will be open, through which a certain steam mass flow rate will be delivered to the components of low pressure condensate heating system (Table 2). A further increase in the turbine load results with opening of second steam extraction (operating point 4, Figure 1), and at high load follows the opening of first extraction. At the highest measured turbine loads, all three steam extractions will be opened, and through all of them, steam mass flow rate will be delivered to all required system components. Therefore, the first steam extraction (operating point 2, Figure 1) from the HPC is the last extraction which will be open at high turbine loads, Table 3.

Steam expansion process in the Mollier h - s diagram for all three main turbine loads in conventional exergy analysis are presented in Figure 3 [114]. Operating points numeration is performed according to Figure 1, while markings a, b and c denote 7.03%, 49.79% and 83.22% of turbine maximum power, respectively. From Figure 3 it can be seen that at low turbine load, steam after expansion (operating point 7a) is still superheated. In marine steam power systems at low load, in the steam flow stream at the main condenser entrance is injected certain amount of water. Injected water cool superheated steam and transferred it to the saturated state (changing of steam aggregate state in condenser at any load can be performed only if the steam is saturated). At higher loads (medium and high load), steam after expansion through the main turbine cylinders is saturated, and it did not require additional cooling (operating points 7b and 7c, Figure 3). It is also important to observe that an increase in turbine load shifts the whole expansion process closer to the saturation line. Such occurrence resulted with a fact that steam at the LPC outlet has higher content of water droplets as turbine load increases.

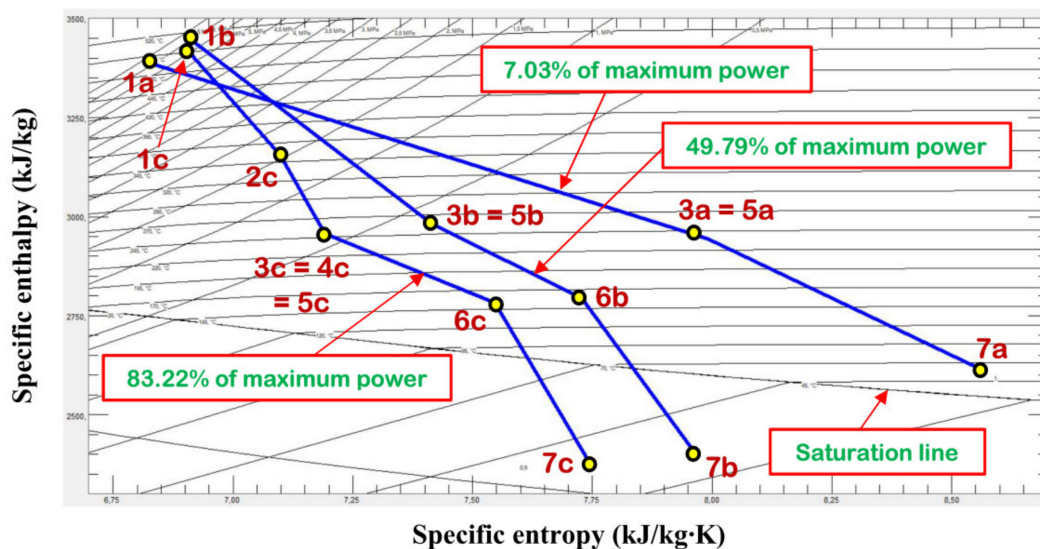


Figure 3. Steam expansion process in Mollier h - s diagram for three observed turbine loads.

5.2. Exergy Analysis by MLP Neural Network Application

The inputs (operating points) in Table 4 have been selected based on the physical relation to each output and part (HPC, LPC and WT) that was modeled. Performing the modeling of all possible combinations of input parameters (operating points) for each desired output would significantly increase the computational complexity. It should also be noted that each operating point consists of measurements for steam temperature, pressure and mass flow rate. In addition to the steam

temperature, pressure and mass flow rate in each of the listed points, each input set also includes the ambient temperature and pressure, with the first combination in all cases only including those two values.

Table 4. Operating points used for regression models for each set of outputs. For each operating point, trained models use steam mass flow rate, temperature and pressure—in addition to ambient pressure and temperature.

Operating Points Combination	HPC * (Outputs: $\dot{E}_{DES,HPC}$, $\eta_{EX,HPC}$)	LPC * (Outputs: $\dot{E}_{DES,LPC}$, $\eta_{EX,LPC}$)	WT * (Outputs: $\dot{E}_{DES,WT}$, $\eta_{EX,WT}$)
1	-	-	-
2	1,2,3,4,5,6,7	1,2,3,4,5,6,7	1,2,3,4,5,6,7
3	1,2,3,4,5	3,4,5,6,7	1,2,3,5
4	1,2,3	4,6,7	2,6,7
5	1,2	5,6,7	1,2,3
6	1,3	6,7	5,6,7
7	2,3	5,6	4,6,7
8	3,4	4,6	3,6,7
9	1,4	5,7	1,2,3,4,5
10	2,4	4,7	2,4,6,7
11	-	-	1,3,7
12	-	-	1,4,7
13	-	-	1,5,7
14	-	-	2,4,6
15	-	-	2,6,7
16	-	-	1,3,5,7
Count	10	10	16

* Operating point numeration refers to Figure 1.

Exergy analysis of the observed steam turbine and both its cylinders by using the MLP neural network is performed as follows:

- (1) By using all collected data, developed mechanical power, exergy destruction and exergy efficiency of each cylinder are calculated as well as the whole turbine at each of the 24 loads with the conventional exergy analysis.
- (2) Results obtained by conventional exergy analysis are then used for MLP training and testing.
- (3) MLP is trained for every hyperparameter combination given in Table 5, which results in a total of 442,368 models when the aforementioned cross-validation process is applied.
- (4) The results of 442,368 models are compared across 72 input/output parameter combinations, given in Table 5, in order to determine the best possible model architecture for each of the aforementioned combinations.

Table 5. Possible values of hyperparameters used in grid search, with the number of the possible hyperparameter values being given in the column titled Total Count.

Hyperparameter	Possible Hyperparameter Values	Total Count
Hidden Layer Sizes	(84,84,84,84)	16
	(84,84,84)	
	(84,84)	
	(84)	
	(42,42,42,42)	
	(42,42,42)	
	(42,42)	
	(42)	
	(21,21,21,21)	
	(21,21,21)	
	(21,21)	
	(21)	
	(84,42,42,21)	
	(42,21,21)	
	(84,42,21)	
	(42,21)	
Activation Function	'relu'	4
	'identity'	
	'logistic'	
	'tanh'	
Solver	'adam'	2
	'lbfgs'	
Learning Rate Type	'constant'	3
	'adaptive'	
	'inverse scaling'	
Initial Learning Rate Value	0.5	4
	0.1	
	0.01	
	0.00001	
L2 Regularization parameter	0.1	4
	0.01	
	0.001	
	0.0001	

The results achieved with each trained MLP model are evaluated using the *MAE* and R^2 metrics described in previous section. This allows the determination of the best models achieved by the MLP method. This also allows the comparison between various operating points in order to determine the best possible measurement combination, or in other words, such a combination which will allow us to obtain the output value with as few operating points, under the condition that the metrics are satisfactory.

Steam operating parameters range (minimum–maximum) in each operating point of the observed main steam turbine (Figure 1) for all 24 measured turbine loads are presented in Table 6. From this table, it can be seen that steam temperature and pressure at the HPC inlet (operating point 1) did not deviate significantly for the variety of turbine loads. This fact shows that both parallel operating steam generators delivers to the HPC steam with the highest temperature and pressure (specified by steam generators manufacturer) in the whole range of main turbine loads. Steam at the LPC outlet (operating point 7) can have high temperature at low turbine loads (which can reach up to 100 °C, Table 6).

Table 6. Steam operating parameters range (min–max) in each operating point for all 24 measured turbine loads.

Operating Point *	Temperature (°C)	Pressure (MPa)	Mass Flow Rate (kg/h)
1	485–513	5.795–6.2	3835–96,789
2	283–365	0.08–1.565	0–3398
3	229–279	0.048–0.593	3835–93,521
4	229–279	0.048–0.593	0–13,202
5	229–279	0.048–0.593	3835–80,319
6	121–169	0.009–0.121	0–4772
7	28.616–100.02	0.00392–0.00561	3835–75,547

* Operating point numeration refers to Figure 1.

Figures 4 and 5 present the ranges of input parameters used in MLP training. Figure 4 shows the values of parameters used as inputs, with subfigure (a) showing the ranges of temperature, (b) the ranges of pressure and (c) the ranges of mass flow rate. The range of values is shown for each operating point, as indicated on the labels, along with the environment value range for temperature and pressure.

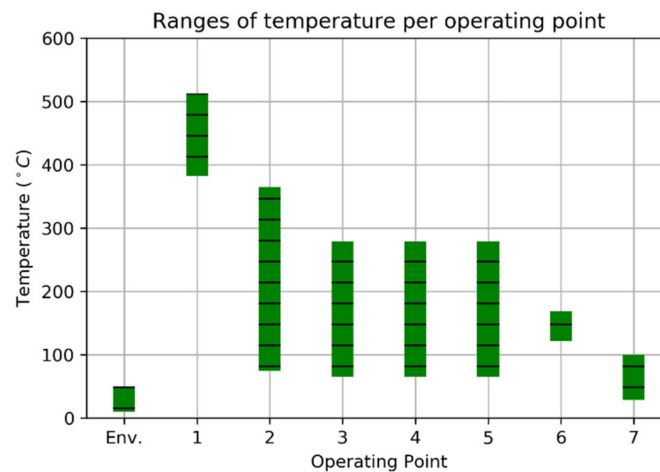
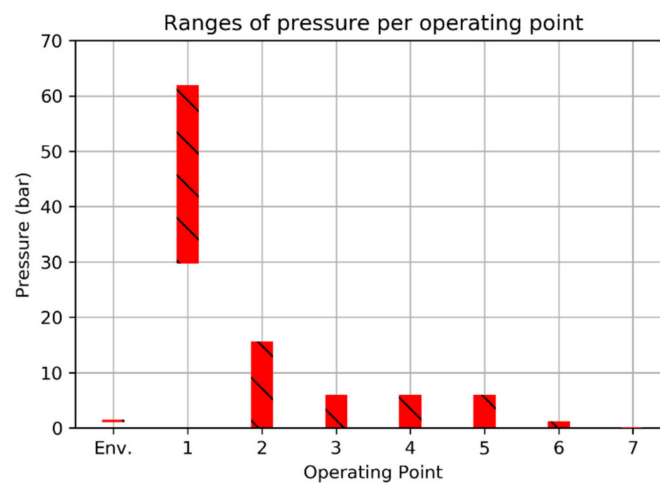
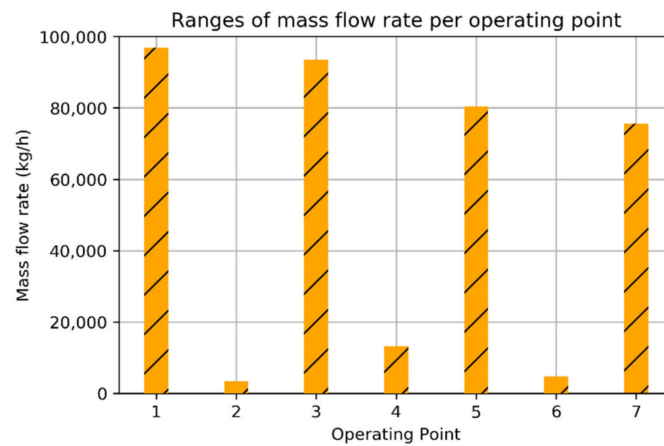
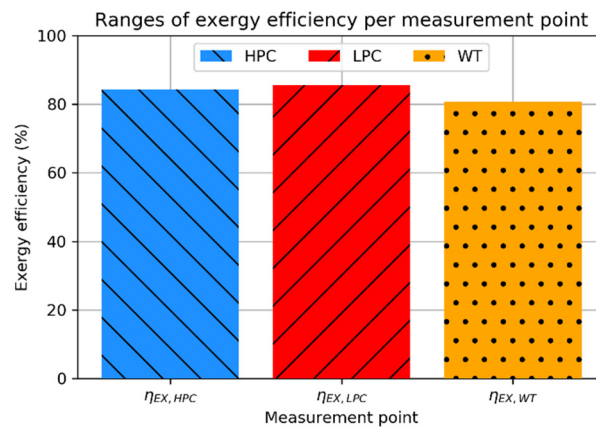
**(a) Ranges of temperature in each operating point.****(b) Ranges of pressure in each operating point.**

Figure 4. Cont.

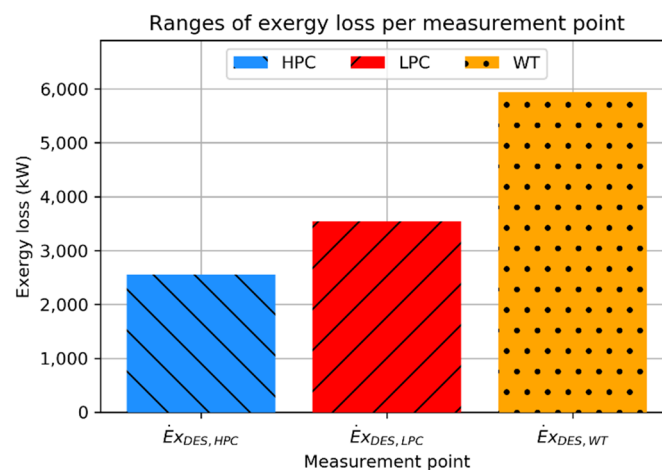


(c) Ranges of mass flow rate in each operating point.

Figure 4. The ranges of measured values used as inputs into the MLP for (a) temperature, (b) pressure and (c) mass flow rate in each operating point, along with the environmental values for temperature and pressure (labeled as Env.).



(a) Ranges of exergy efficiency in each output point.



(b) Ranges of exergy loss in each output point.

Figure 5. The range of measured values used as outputs into the MLP for (a) exergy efficiency and (b) exergy loss measured for HPC, LPC and WT.

Figure 5 shows the range of output values, with subfigure (a) demonstrating the range of exergy efficiency values, while the subfigure (b) shows the exergy loss (exergy destruction) at each measurement point (HPC, LPC and WT).

It should be stated that exergy efficiency and exergy loss (exergy destruction) range starts from zero for the whole observed turbine and each of its cylinders. The reason of such occurrence is the first observed turbine load (of 24 overall loads). The first observed load is actually the heating of turbine (before start). In that load, the turbine and its cylinders did not produce useful power, so the exergy efficiencies and losses are equal to zero (losses are so small that it can be neglected).

5.3. Measuring Equipment

Measurements of steam temperature, pressure and mass flow rate in each operating point from Figure 1 are performed with a standard measuring equipment, calibrated and already mounted inside the power plant. That measuring equipment is used for the main steam turbine process control and regulation during exploitation. The list of used measuring equipment is presented in Table 7, while the detail specification of each measuring device can be found on the manufacturer website (provided in the list of references). Details related to measurement equipment accuracy and range of operation can be found in the Appendix A at the paper end. The measurement error did not have a significant influence on the obtained exergy analysis results.

Table 7. Used measuring equipment.

Operating Point *	Temperature (Immersion Probes) [116]	Pressure (Pressure Transmitters) [117]	Mass Flow Rate (Differential Pressure Transmitters) [118]
1	Greisinger GTF 601-Pt100	Yamatake JTG960A	Yamatake JTD960A
2			
3			
4	Greisinger GTF 401-Pt100	Yamatake JTG940A	Yamatake JTD930A
5			Yamatake JTD920A
6			
7			Yamatake JTD910A

* Operating point numeration refers to Figure 1.

6. Results and Discussion

This section will present the results obtained first by the conventional exergy analysis, followed by the results obtained by the application of described AI methodology.

6.1. The Results of the Conventional Exergy Analysis

In the conventional exergy analysis of any steam turbine, from measured steam operating parameters firstly should be calculated produced mechanical power. For the case of this particular marine steam turbine, produced mechanical power is calculated not only for the whole turbine, but also for both turbine cylinders (HPC and LPC), see Figure 6. An increase in turbine load is followed by the increase in developed mechanical power of the whole turbine. However, from Figure 6, the share of each turbine cylinder in the cumulative developed mechanical power is interesting and important to observe. At low load, the dominant mechanical power producer is HPC. An increase in turbine load results in a change in cylinder developed mechanical power share—at middle load the dominant mechanical power producer is LPC. At the highest measured loads, the share of both turbine cylinders in cumulative developed mechanical power is approximately the same; therefore, at the highest loads each cylinder develops approximately 50% of cumulative power. The same general conclusion about

this type of marine steam turbines related to cylinder share in cumulative developed mechanical power at various loads can be found in the literature [66].

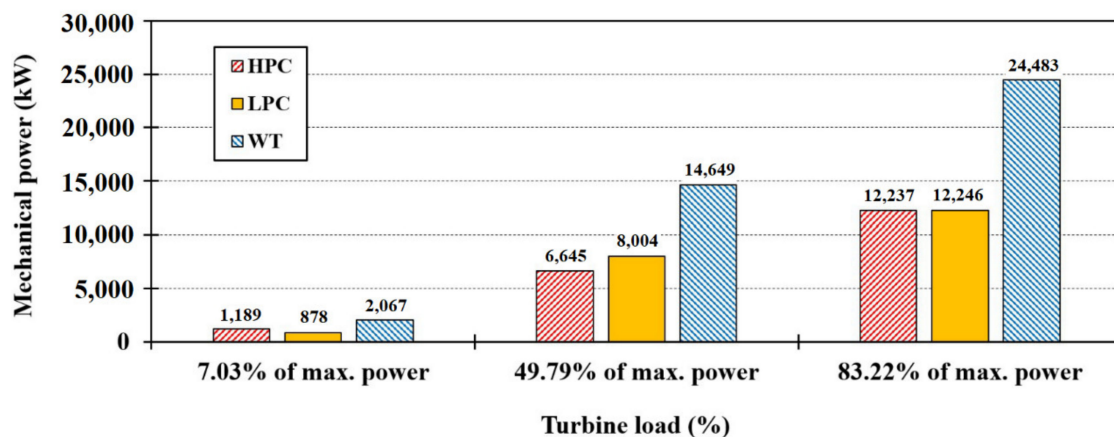


Figure 6. Mechanical power developed by the main turbine and each of its cylinders at three observed loads.

For three observed turbine loads in the conventional exergy analysis, developed mechanical power of HPC and LPC increases from 1189 kW and 878 kW at low load, to 6645 kW and 8004 kW at middle load and finally to 12,237 kW and 12,246 kW at high turbine load, respectively (Figure 6). It should be noted that developed mechanical power at each load presented in Figure 6 and calculated in each of 24 turbine loads is mechanical power calculated according to measured steam operating parameters and real (polytropic) steam expansion process throughout each cylinder. According to Figure 1, the mechanical power used for propulsion propellers drive in each turbine load is lower than the mechanical power calculated and presented in this analysis. The reason of such a difference is, as mentioned earlier, neglecting mechanical and other losses in the bearings, shafts and main gearbox.

Conventional exergy analysis at three observed turbine loads results with exergy destruction (exergy loss) and exergy efficiency of the whole main steam turbine and both of its cylinders, Figure 7. Comparison of Figures 6 and 7 shows that the developed mechanical power and exergy destruction of each cylinder and the whole turbine are directly proportional—higher developed mechanical power results in higher exergy destruction and vice versa. It is interesting to note that at a high load (83.22% of maximum power), regardless of the low difference between HPC and LPC developed mechanical power, LPC exergy destruction is significantly higher in comparison to HPC. Exergy destruction of the whole turbine increases during the load increase (proportional to developed mechanical power)—from 1380.09 kW at the low load, to 4437.86 kW at the middle load and finally to 5814.43 kW at the high load.

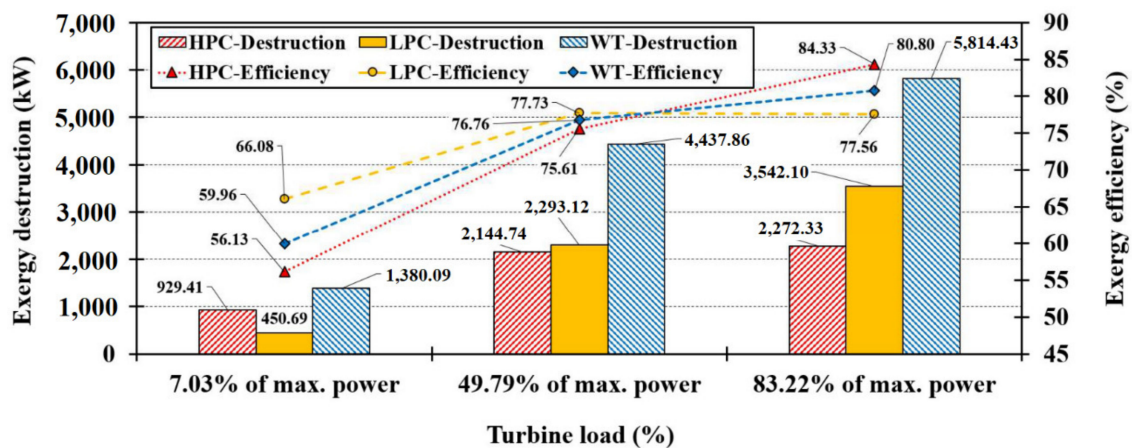


Figure 7. Exergy destruction and exergy efficiency of the main turbine and each of its cylinders at three observed loads.

Exergy efficiency results at three observed turbine loads in conventional exergy analysis show that an increase in turbine load increases the exergy efficiency of the whole turbine and each of its cylinders. The only deviation from this statement can be seen for the LPC, of which exergy efficiency slowly decreases from middle to high load (from 77.73% to 77.56%). Such a trend for LPC cannot be taken as relevant because the difference in exergy efficiency between middle and high load is so small that it can be the result of measurement equipment accuracy. By observing turbine cylinders, for low and high load a reverse proportionality between exergy destruction and exergy efficiency is valid—higher cylinder exergy destruction results in lower exergy efficiency. The mentioned reverse proportionality is not valid for the middle turbine load, where LPC, which has higher exergy destruction than HPC, also has higher exergy efficiency. An increase in the whole turbine load results in a simultaneous increase in its exergy efficiency—from 59.96% at a low load, followed by 76.76% at a middle load, to 80.80% at a high load (Figure 7).

In conclusion to previously described observations can be stated that the main marine steam turbine operation should be maintained at a high load where the whole turbine develops high mechanical power and has the highest exergy efficiency. Simultaneously, at a high load it should be taken into consideration that the whole turbine exergy destruction will be the highest, in comparison to lower loads. At a high load, both turbine cylinders will almost equally participate in cumulative developed mechanical power, but the exergy efficiency of HPC will be higher and its exergy destruction will be lower in comparison to LPC.

6.2. Exergy Analysis Results by MLP Neural Network Application

The results of MLP analysis are presented below. In order, the results for HPC, LPC and WT exergy destruction and efficiency are given. The graphs present the best results achieved using MLP per each given input combination, for each of the separate goals. In addition to MAE, Mean Relative Error (MRE) is used for presentation in order to demonstrate the error as a percentage of the range of the measured output. The results are not given for the case in which no input operating points have been used, using only ambient pressure and temperature, as the models for all possible hyperparameter combinations in all possible cases have failed to converge to a solution and as such have not provided any viable or meaningful results. The failure to converge in such a case suggests that such a regression, using only the ambient values, is insufficient for the desired outputs due to low or non-existent correlation between the ambient values and the desired outputs.

As for the acceptable error range, any MRE value that is smaller than 2% of the output range for a given output is considered to be acceptable, as this is precise enough estimation for the practical purposes in determining the exergy destruction and efficiency of a turbine in the marine environment. In the same manner, any R^2 value that is higher than 0.95 is considered within the acceptable range.

This means that all models obtained with a certain input combination that have achieved an R^2 value higher than 0.95 and an MRE lower than 2% are to be considered when the final model selection is performed.

For all figures in this subsection, numbers or ranges written on the abscissa (combination of input parameters) are related to operating points presented in Figure 1.

MAE and MRE scores in the case of HPC exergy destruction (exergy loss) estimation display low errors across all inputs ($MRE < 2\%$), but there are some outliers. Namely, input combinations lacking the operating point 2 (3,4; 1,4; 1,3) display the highest error, suggesting that operating point 2 is necessary to achieve a low model error in this case. This is shown in Figure 8.

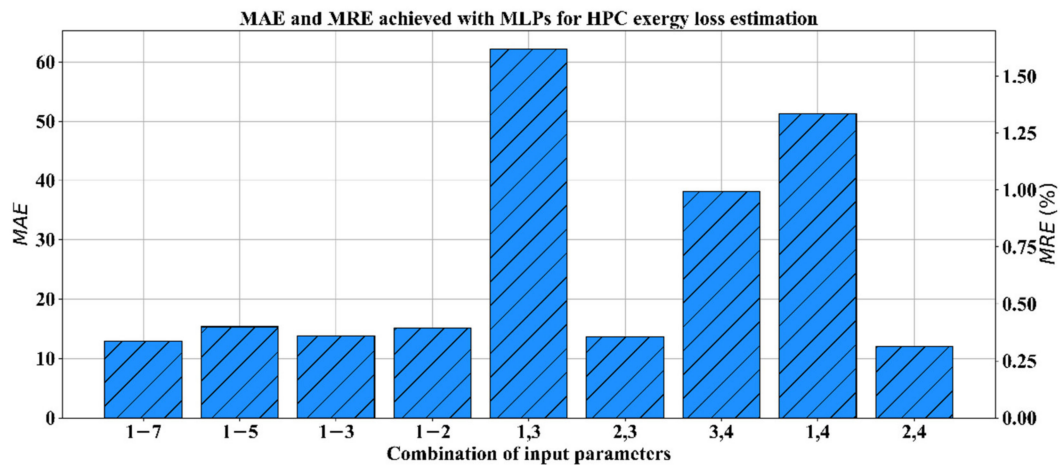


Figure 8. MAE and MRE values for HPC exergy destruction (exergy loss).

Figure 9 shows the R^2 scores achieved being high across all input combinations, with all of them achieving scores in excess of 0.99. These suggest that all the input combinations may be used for modeling, since all models track the outputs well, as long as a higher error of some models does not present an issue. Still, it is evident that those combinations of operating points which do not include the operating point 2 achieve a lower R^2 score, which corresponds with the larger errors provided by those models. This further shows the importance of the operating point 2 in the modeling of HPC exergy loss—if higher precision than the one sought in this document is needed.

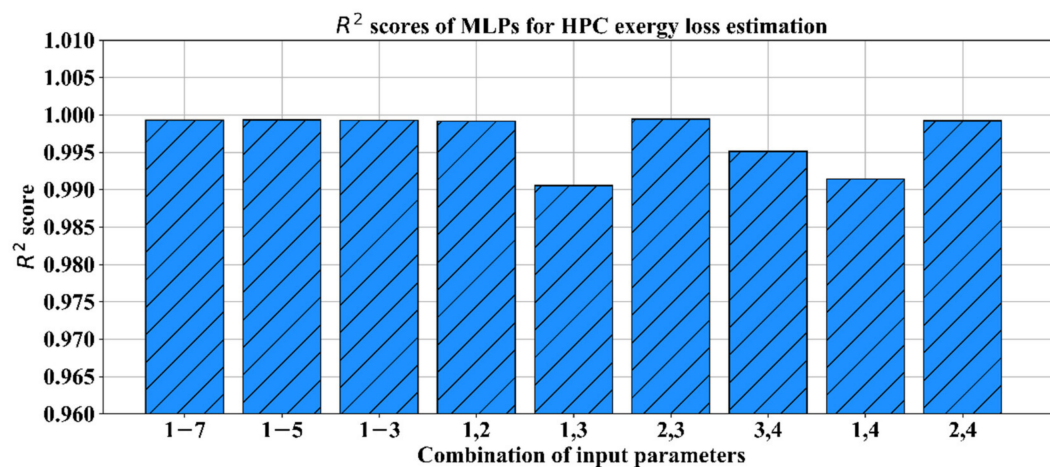


Figure 9. R^2 values for HPC exergy destruction (exergy loss).

While observing the MAE and MRE for HPC exergy efficiency estimation, given in Figure 10, it can be seen that all the input combinations achieve very low errors, namely below 1%. Interestingly, operating point 2, which seemed to have a large benefit, does not have as much

importance. It seems that this role is replaced by the operating points 3 and 4 used in all combinations that achieve lower errors. As with the previous models, all the models here achieve *MAE* scores low enough to be considered for use.

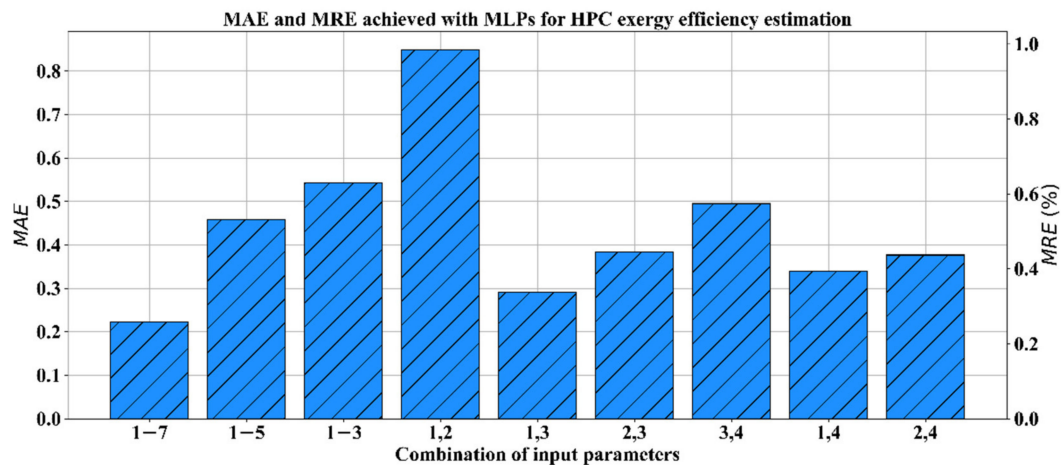


Figure 10. *MAE* and *MRE* values for HPC exergy efficiency.

Figure 11 shows that R^2 scores achieved for HPC exergy efficiency models are high, except in the case of input combination 1,2. Due to this combination being the only one which does not include operating points 3 or 4, it suggests the importance of these inputs in HPC exergy efficiency model as the previous graph. In line with the *MAE* scores, the R^2 scores achieved are high enough ($R^2 > 0.95$) to be considered usable in modeling HPC exergy efficiency.

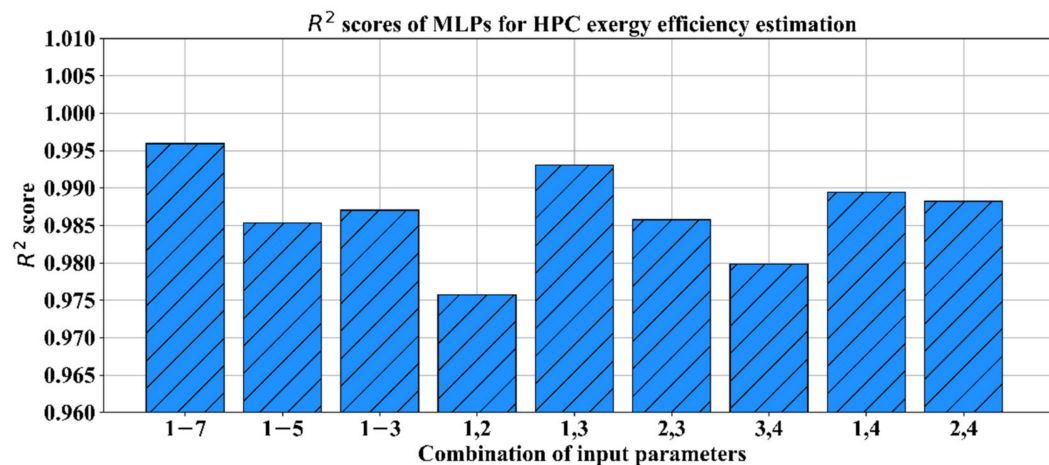


Figure 11. R^2 values for HPC exergy efficiency.

While all the input combinations provide satisfactory metric values in terms of *MRE* ($MRE < 2\%$) for HPC exergy destruction and exergy efficiency estimators, it can be seen that there are some that do not achieve as high an R^2 value for exergy efficiency estimation ($R^2 > 0.99$). Namely, only input combinations which achieve R^2 scores 0.99 or higher are 1-7; 1,3 and 1,4. It can also be seen that R^2 scores of those operating point combinations which achieve a higher error are lower, which is to be expected.

By observing all the achieved scores for the output models of HPC it can be shown that the best scores are achieved, for both exergy efficiency and exergy destruction, when the input operating point combinations used are 1,4; 2,4; 2,3 and 1-7. These operating point combinations are obtained by considering both errors and R^2 value scores for both exergy efficiency and exergy loss, and while

they may not present the best possible model for an individual output, a high enough performance is evidenced in both observed output cases for HPC.

Figure 12 demonstrates the best MAE and MRE achieved by the MLP for each input combination in the case of exergy destruction estimation for LPC. It can be seen that the best results are achieved when all the inputs are used (1–7), with comparable results being achieved for all the input combinations, which include operating points 5, 6 and 7. Still, all the operating point combinations provide a satisfactory error below 1.5%, signifying that they may all be used in modeling the LPC exergy loss.

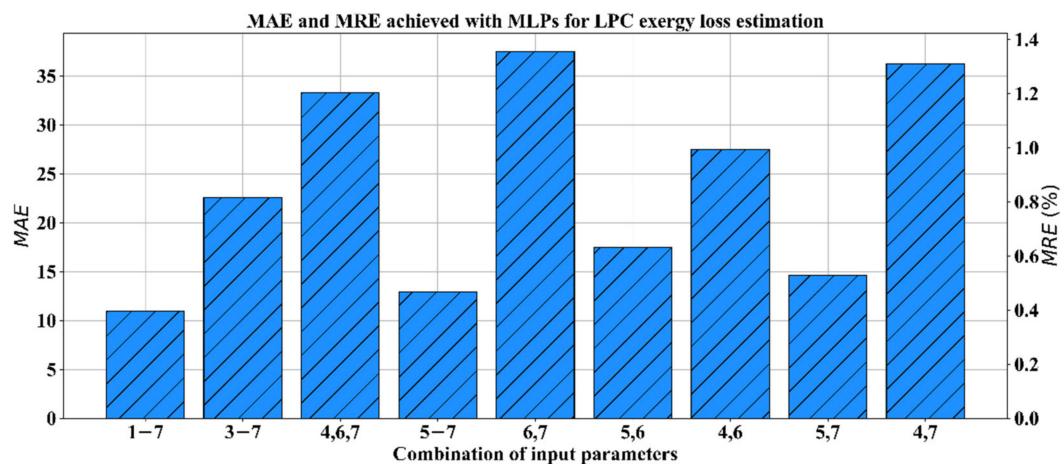


Figure 12. MAE and MRE values for LPC exergy destruction (exergy loss).

While observing the R^2 scores for LPC exergy destruction estimation presented in Figure 13, it can be seen that all input combinations achieve relatively high R^2 scores ($R^2 > 0.95$), meaning that all the models may be used in the LPC exergy destruction modeling. It should be noted that the input combination 5–7, despite a relatively low MAE in comparison to other results, has the lowest R^2 score. This points to the fact that, despite achieving a low error, this input combination does not explain all the variations in the test data. It can be concluded that this is due to the lack of information being contained within this input combination. Through comparison with the input combination of operating points 5 and 7, which has achieved a higher score, it can be concluded that the inclusion of operating point 6 as an input is actually detrimental to the model, lowering instead of increasing performance.

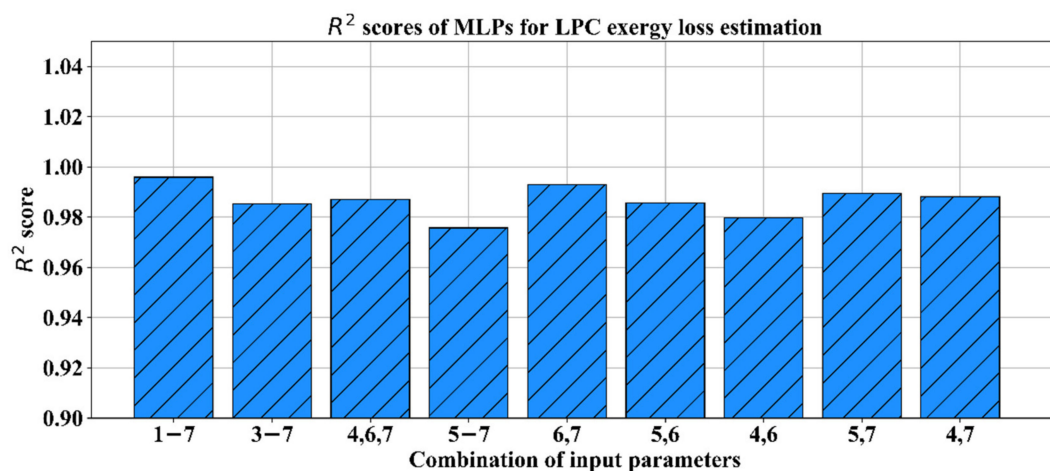


Figure 13. R^2 values for LPC exergy destruction (exergy loss).

For the model of LPC exergy efficiency, as in the previous case the best results are achieved when all inputs are used together (case 1–7), with comparable results being achieved for input combination 3–7. Despite this, all input combinations have achieved a low error ($MRE < 1\%$), with the highest error

occurring when input combination 6,7 is used. Interestingly, the input combination 5–7 shows a lower error than combination 5,7, meaning that the inclusion of operating point 6 is beneficial in this case, but the use of the measurements in operating point 5 is largely beneficial to it. Because of this, we can conclude that the combination of values in operating points 5 and 6 is important to achieve extremely low scores in the LPC exergy efficiency modeling. However, as with the previous models, all the error values are low enough to conclude that all models may be used. These results are shown in Figure 14.

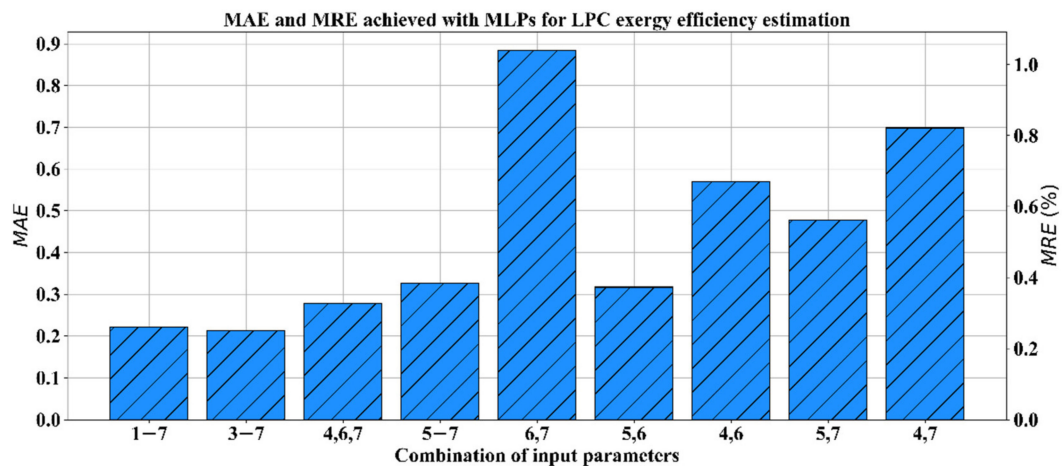


Figure 14. MAE and MRE values for LPC exergy efficiency.

As for the R^2 scores of the model for LPC exergy efficiency in Figure 15, it can be seen that the lowest score is achieved by the input combination 6,7, which has the highest error (as can be seen in Figure 14). Still, this combination, and all others, provide a quality enough model of LPC exergy efficiency. This points to the lack of information necessary for a higher quality model when these inputs are used. Higher quality models being achieved in all other cases, which points to the fact that LPC exergy efficiency models require the use of operating point 4 or 5, in order to achieve higher regression quality, and the scores achieved show that operating points 5 and 6—when used in unison—provide enough information for MLP to successfully converge to a high-quality solution.

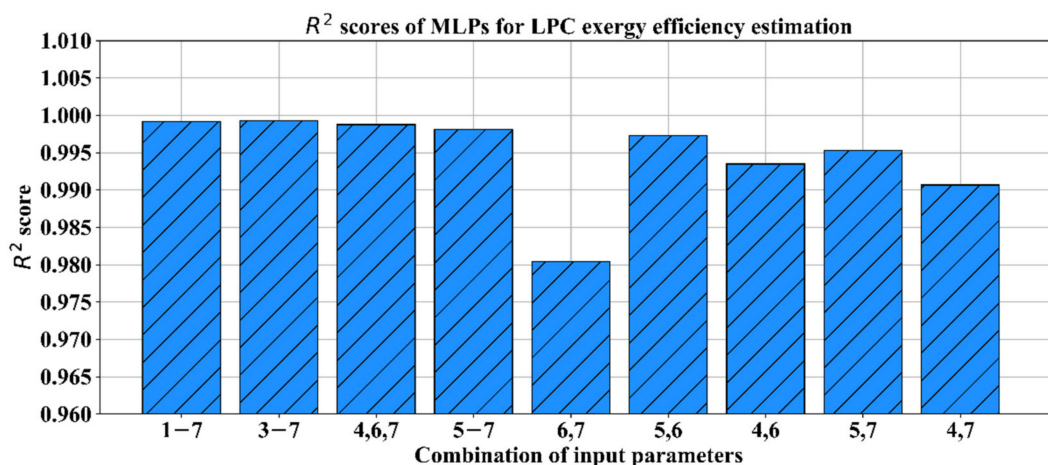


Figure 15. R^2 values for LPC exergy efficiency.

When observing the LPC exergy destruction and exergy efficiency estimation outputs (Figures 12–15), it can be seen that the best results are achieved when all the inputs are used, but satisfactory results are achieved for all input combinations with R^2 values in excess 0.97, and MRE below 1.5%. Observing all the scores points towards the fact that the best results for the LPC outputs,

including both exergy destruction and exergy efficiency, are obtained when points used are 1–7; 5–7; 4,6,7 and 4,7.

Figure 16 demonstrates MAE and MRE values obtained by the models for WT exergy loss estimation. It can be seen that all the error values are extremely low. The only input combination which exceeds the error of 1% is the combination of operating points 1–3,5, which achieves an error below 1.2%. However, such an error is still within the acceptable error range, meaning that all the models of WT exergy loss achieve satisfactory performance in regards to the MAE.

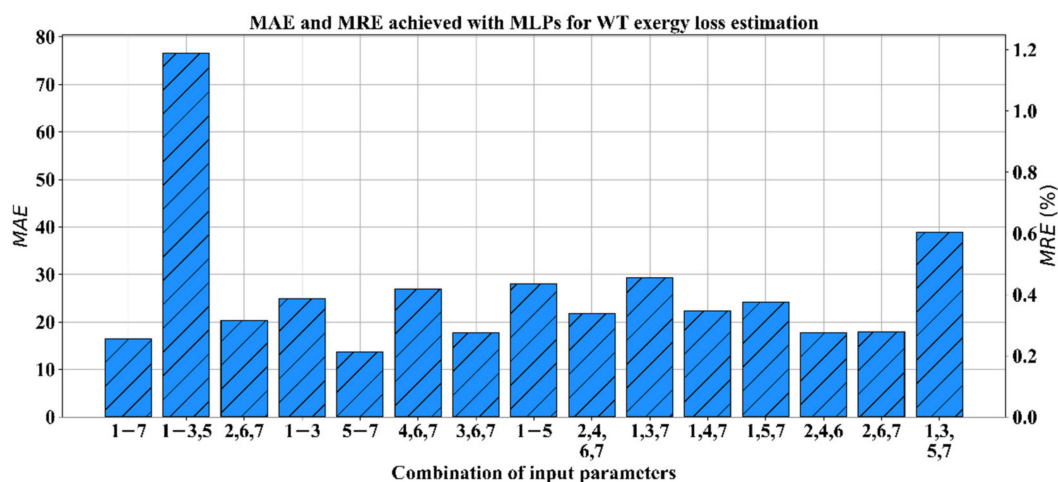


Figure 16. MAE and MRE values for WT exergy destruction (exergy loss).

Figure 17 demonstrates the R^2 scores achieved by the WT exergy loss estimation fall in line with the MAE and MRE results achieved, with all the inputs achieving R^2 scores in excess of 0.985; meaning all are high enough to be considered for modeling. The lowest score is achieved by the input combination 1–3,5 which, with the value of 0.99, is still inside the acceptable range.

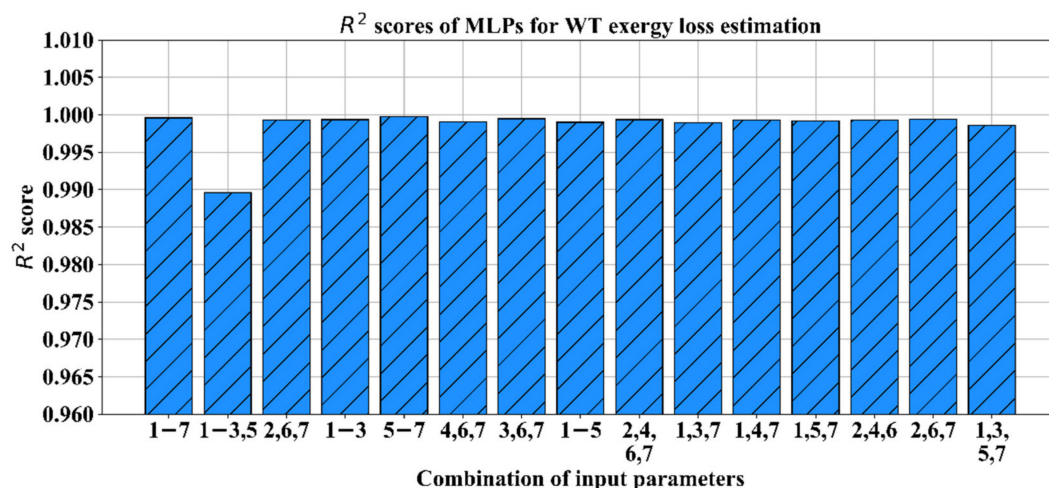


Figure 17. R^2 values for WT exergy destruction (exergy loss).

Observing both scores for WT exergy loss, it can be concluded that all models achieve similar high performance, with the exclusion of operating points 1,3,5,7 and 1–3,5, which achieve comparatively poorer scores. Still, all the model's scores fall well within the satisfactory ranges, indicating that it is possible to use them for the given task.

Through observing Figure 18, MAE and MRE of the WT exergy efficiency estimation can be seen. The output combination 1–5 achieves the lowest results, which is, interestingly, higher than the input combinations of 1–3,5 and 1,3,5,7, which do not include the operating point 4. This signifies that

operating point 4 may be detrimental in this particular case, but not so much that its inclusion should be avoided, considering the error introduced by it is at its maximum below 0.3%. Due to all *MRE* values being below 0.5, this should not have a large influence on model selection.

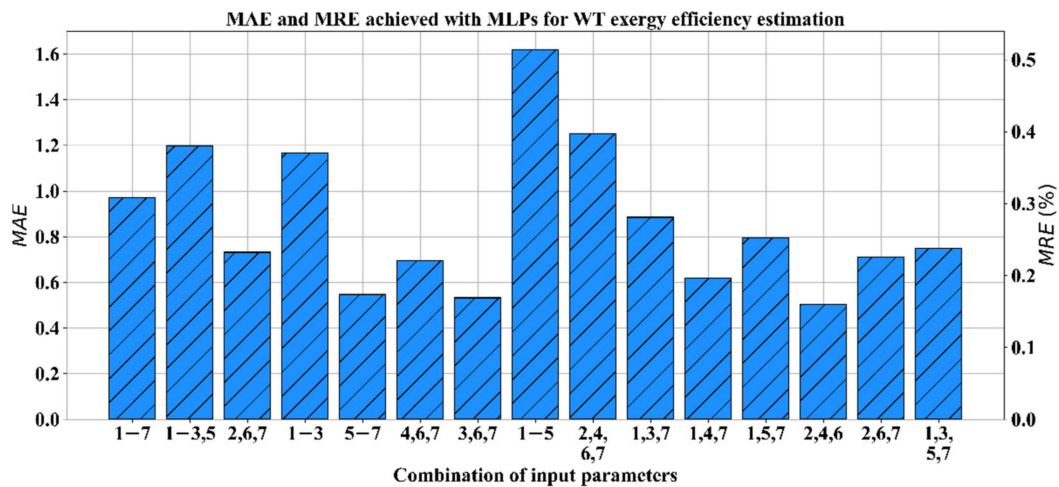


Figure 18. MAE and MRE values for WT exergy efficiency.

Figure 19 shows the R^2 values achieved by the models for WT exergy efficiency estimation. The figure shows that the R^2 scores achieved mostly fall into line with the MAE achieved, with those models that show a higher error, also showing a lower R^2 score, but with less drastic differences. It can be seen that all the scores are in the excess of 0.99, which confirms that all the models are of high quality and that models with all the input combinations may be used during the model selection.

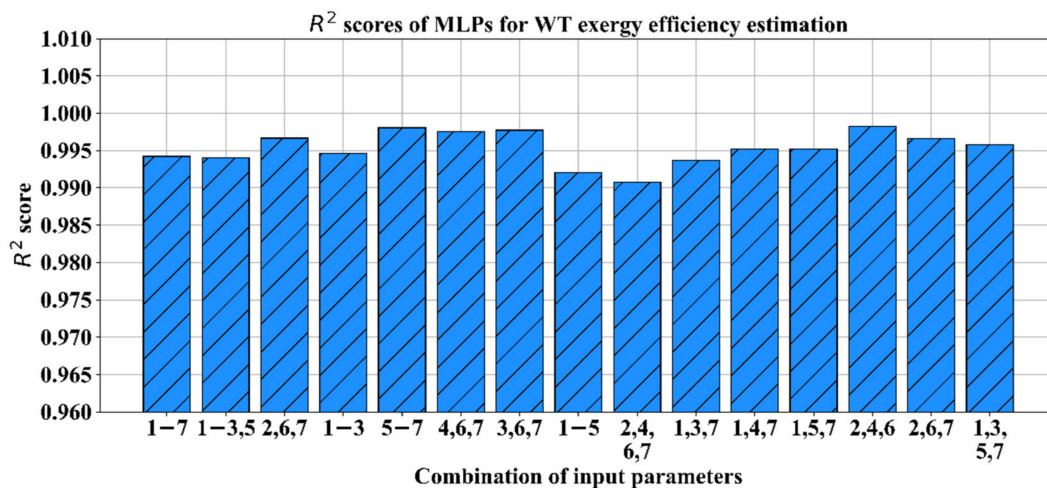


Figure 19. R^2 values for WT exergy efficiency.

In the case of the output analysis of the whole turbine, it can be seen that error values are extremely low, except for the model of exergy destruction when the input combination of operating points 1–3,5 is used. When the input of 1–3,5 operating points is used, the R^2 value drops below 0.99 and *MRE* grows above 1%. While these values are still within the limits of satisfactory results it can be concluded that they present the worst input combination in term of WT exergy destruction modeling, but may still be used if necessary. The best results achieved for both WT exergy destruction and efficiency are obtained when the following input parameters are used: 1–7; 1,4,7; 5–7; 2,4,6.

Considering that all the used operating point combinations achieve MAE of below 2% for the output value range and R^2 score higher than 0.95, all may be used for modeling the required outputs. For example, if a situation is observed in which the measuring equipment may already exist at the given

points and installing it in different ones may pose a difficulty, using a model with slightly poorer scores (but still within the satisfactory range) can be a good choice. All the input operating point combinations which achieve quality models show the importance of including domain experts in the artificial intelligence-based research. In the presented research, this allowed for lowering the number of input combinations that were tested and consequentially for a lower computational complexity—while still generating useable models.

By observing the presented graphs, the best input combination can be determined. This can be done by cross referencing the best scores achieved in order to find the combination of inputs that provides the best scores. For example, while the best scores across all the observed cases are obtained when input combinations 1–7 are used, this does not lower the amount of operating points needed. Due to all of the output metrics falling well within the satisfactory error range, the selection can concentrate on finding such a combination of input operating points, which allows for an as low as possible number of operating points. If the goal is to achieve satisfactory measurements with as few operating points as possible, then it can be concluded that this combination is 1, 4 and 7—or namely by utilizing operating points 1 and 4 for HPC, 4 and 7 for LPC and 1,4,7 for WT. The respective values achieved for each cylinder and the whole turbine are given in the graphs below.

Selected operating points (1, 4 and 7) reduce the number of the required measurements for more than half (from 21 to 9 overall measurements of the steam mass flow rate, temperature and pressure). Selected operating points are the most dominant operating points related to the marine steam turbine operation because steam operating parameters at the turbine inlet and outlet also gives information about steam generators and main steam condenser operation. Additionally, knowing steam operating parameters in only one extraction, mounted between turbine cylinders, will be satisfactory for MLP estimation of turbine exergy analysis parameters. Therefore, MLP application can be very beneficial for reducing the costs of measurement and regulation equipment. The same idea, applied to the main marine steam turbine and its cylinders in this paper, can be applied to the whole marine steam propulsion plant.

Figure 20 demonstrates MAE and MRE of the selected input combinations. All the selected models achieve the errors of below 1.5%, with the models for HPC and LPC exergy destruction estimation achieving MRE of 1.2%, and the WT exergy destruction model achieving the MRE of 0.6%.

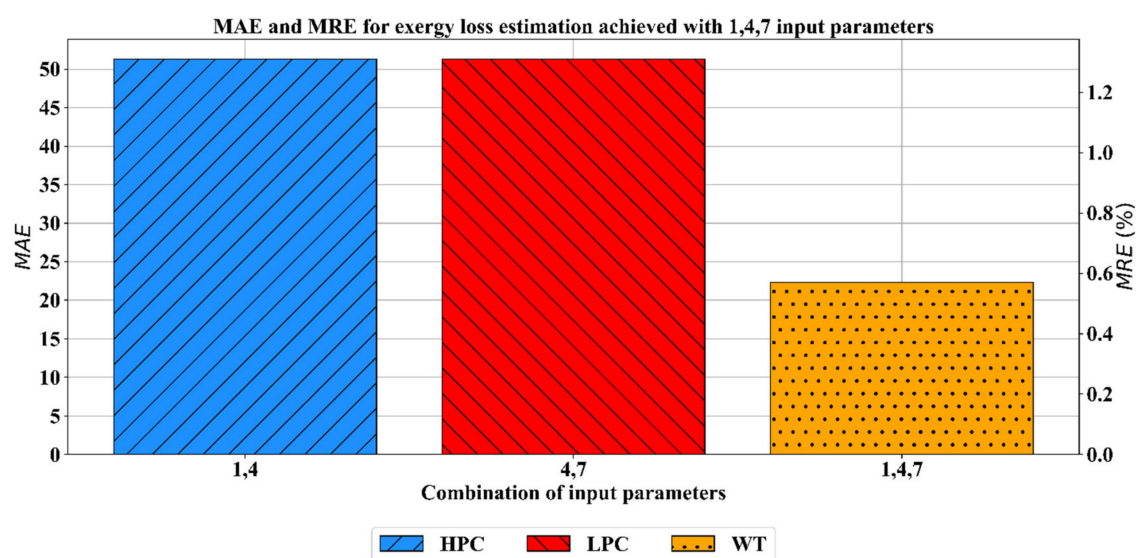


Figure 20. MAE and MRE values of the selected input combination (1,4,7) for exergy destruction (exergy loss).

R^2 scores for exergy loss of the whole turbine and each cylinder, presented in Figure 21, show that the models for HPC and WT achieve high fidelity with R^2 scores in excess of 0.99. The lowest R^2

score is achieved by the LPC model which reach the R^2 score of 0.97. While lower than some scores, when coupled with the low error seen in Figure 20, it can be concluded that this model is satisfactory. The importance of using multiple metrics when evaluating the artificial intelligence-based models is shown here, as models with a high R^2 value may achieve a critically low error or vice-versa. Similarly, a model that may seem to achieve a relatively poor score when a single metric is used may show good performance when evaluated with other metrics, leading to the conclusion that such a model is still usable (providing all the metrics are within the satisfactory ranges).

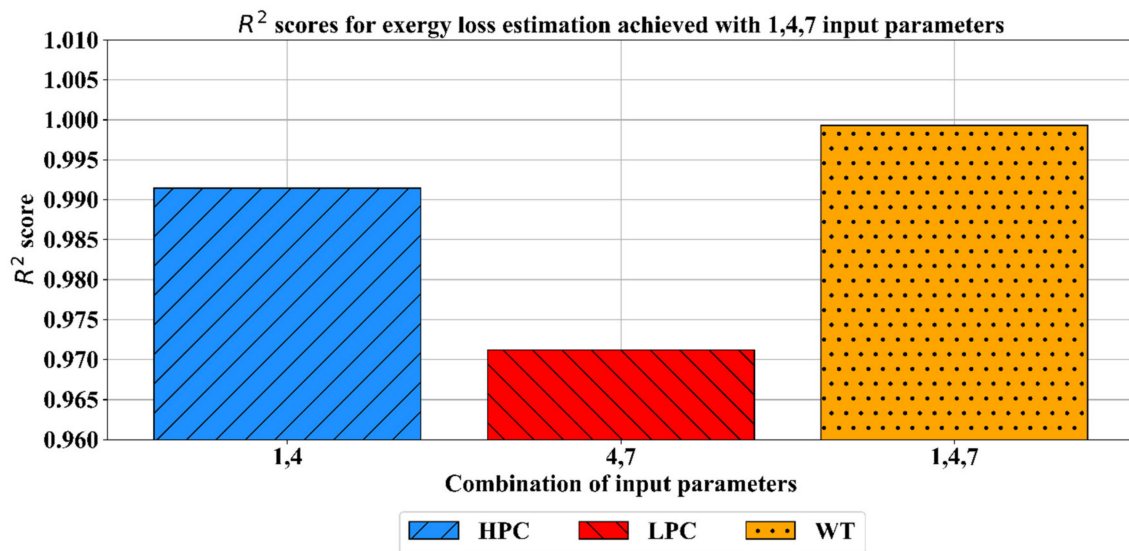


Figure 21. R^2 values of the selected input combination (1,4,7) for exergy destruction (exergy loss).

By observing Figure 22, MAE and MRE values of selected models for exergy efficiency can be seen. As shown, all the models achieve a low error (below 1%), with the error for the HPC exergy efficiency model being less than 0.5% and WT exergy efficiency model showing the error of below 0.3%. The highest error is achieved for the LPC exergy efficiency model, which achieves an error of 0.8%, what is well within the satisfactory error range.

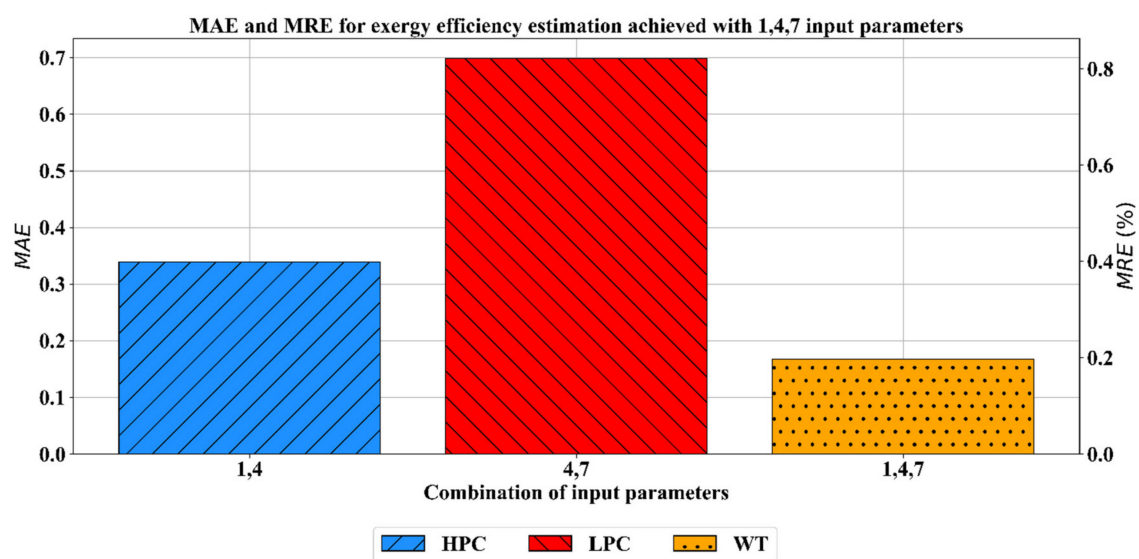


Figure 22. MAE and MRE values of the selected input combination (1,4,7) for exergy efficiency.

Finally, Figure 23 demonstrates the R^2 scores for the exergy efficiency estimation. With all the scores being in excess of 0.99, it can be concluded that all the selected models for exergy efficiency

estimation of LPC, HPC and WT achieve satisfactory results. All the results are relatively close, with the lowest being the result for the HPC exergy efficiency model, achieving a score just slightly lower than 0.99.

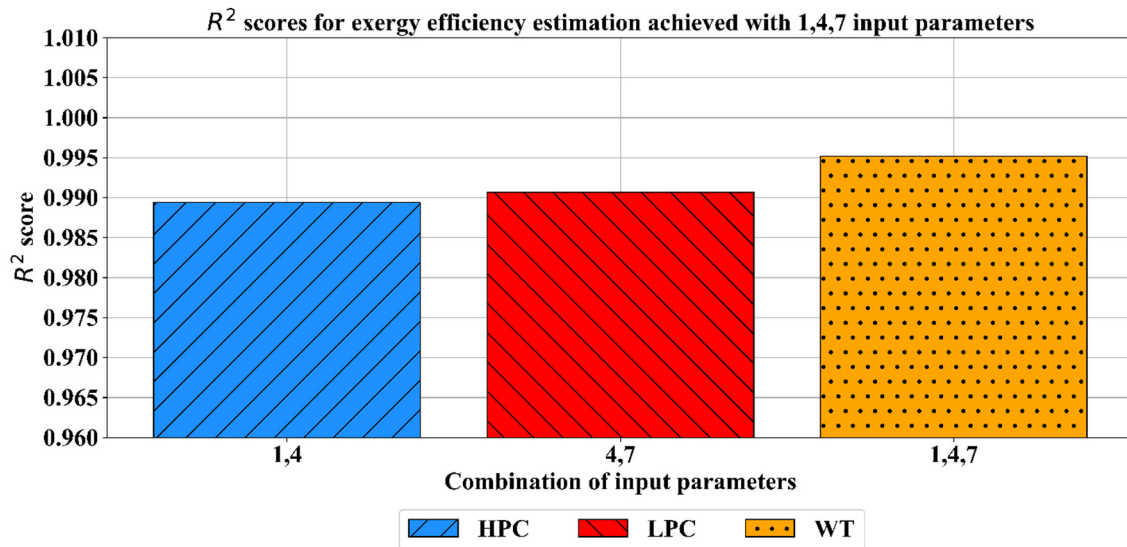


Figure 23. R^2 values of the selected input combination (1,4,7) for exergy efficiency.

While individually the input parameters may not have the best scores achieved, they all achieve relatively high scores. Considering that errors of models are below 1.5% when these input combinations are used, this is satisfactory for the measurement needs, especially since only three operating points are used. The hyperparameter values and numerical values of metrics for exergy destruction achieved are given in Table 8, and the values for the hyperparameters used in the best models are presented in Table 9. In the same way, values are given for exergy efficiency in Tables 10 and 11.

Table 8. Metrics achieved by selected operating points, for modeling of exergy destruction.

Operating Point	R^2	+/-	MAE	+/-
1,4 (HPC)	0.9914541639	0.02378781401	51.27713297	36.21271356
4,7 (LPC)	0.9712139368	0.09161658705	36.22307872	50.75836187
1,4,7 (WT)	0.9992643028	0.00172978046	20.44955009	12.32598431

Table 9. Hyperparameters used for best solutions achieved in selected operating points, for modeling of exergy destruction.

Operating Point	1,4 (HPC)	4,7 (LPC)	1,4,7 (WT)
Activation Function	ReLU	ReLU	ReLU
L2 Regularization	0.001	0.01	0.1
Hidden Layer Sizes	(84)	(84, 84, 84, 84)	(84, 84, 84, 84)
Learning Rate Type	Adaptive	Constant	Adaptive
Initial learning rate	0.1	0.01	1e-05
Solver	LBFGS	LBFGS	LBFGS

Table 10. Metrics achieved by selected operating points, for modeling of exergy efficiency.

Operating Point	R^2	+/-	MAE	+/-
1,4 (HPC)	0.9894154031	0.03141286439	0.3393632265	0.3058120431
4,7 (LPC)	0.9906770758	0.02055184947	0.6985228666	1.1429986910
1,4,7 (WT)	0.9951798924	0.01330619104	1.6066829045	0.0133061910

Table 11. Hyperparameters used for best solutions achieved in selected operating points, for modeling of exergy efficiency.

Operating Point	1,4 (HPC)	4,7 (LPC)	1,4,7 (WT)
Activation Function	ReLU	ReLU	ReLU
L2 Regularization	0.1	0.1	0.1
Hidden Layer Sizes	(84,42,21)	(84,84,84)	(84,84,84,84)
Learning Rate Type	Constant	Constant	Adaptive
Initial learning rate	0.1	0.01	1e-5
solver	LBFGS	LBFGS	LBFGS

Table 8 demonstrates the scores achieved for the exergy destruction with the selected input operating point combinations. It can be seen that the HPC and WT outputs modeled with operating points 1,4 and 1,4,7, respectively, achieve R^2 scores in excess of 0.99, while the model for the LPC output, modeled with operating points 4,7, achieves a lower, but still satisfactory, R^2 score of 0.97. Maximal error ranges achieved during the cross-validation have also been provided next to the average of all 10 validation scores for both R^2 and MAE.

Table 9 provides the hyperparameters used to obtain models that have provided the solutions within the Table 8. The values of hyperparameters presented within Table 9 are a subset of hyperparameters provided within Table 5. Only the hyperparameters which have been used to obtain the best selected models are presented for brevity. It can be seen that a relatively large network, of 4 layers with 84 neurons each, has been used in the case of LPC and WT exergy destruction models, while the HPC exergy destruction model utilized a significantly smaller network—consisting of a single layer with 84 neurons. All the best models for exergy destruction used LBFGS solver and ReLU activation function.

Table 10 presents the scores for the exergy efficiency models, providing R^2 and MAE scores for LPC, HPC and WT models (input combinations being 1,4, 4,7 and 1,4,7 respectively). The table demonstrates that the R^2 scores achieved are in excess of 0.99 for LPC and WT exergy efficiency models, while the HPC model achieved the average R^2 score of 0.989 after the cross-validation process. MAE scores demonstrate an error of less than 1% of exergy efficiency for HPC and LPC models. MAE score grows to 1.6% for WT exergy efficiency, but the error is still within the previously stated satisfactory error range. As was the case in Table 8, the maximal error ranges obtained during the cross-validation are provided next to the obtained average R^2 and MAE scores in Table 10.

Hyperparameters used to obtain the solutions in the case of exergy efficiency are given in Table 11. As in Table 9, it can be seen that ReLU activation function and LBFGS solver have been used in all cases. Interestingly, the initial learning rates for each individual input operating point combination are the same as they were for exergy destruction models, indicating a similarity between the two regression problems. By observing the hidden layer size hyperparameter, it can be seen that the model for HPC exergy efficiency also required a lower number of neurons in comparison to the LPC and WT exergy efficiency models, as it did in the models of exergy destruction. Still, the number of neurons for HPC exergy efficiency model is much closer to the LPC and WT exergy efficiency models than it was the case for exergy destruction, indicating closer complexity in the problems.

From the hyperparameter tables (Tables 9 and 11), it can be seen that all solutions tended towards the larger number of hidden neurons. This, coupled with a high initial learning rate which was kept either constant or adaptive, signifies a hard to model problem [84]. It can also be seen that some models, namely the ones pertaining to the HPC exergy destruction and exergy efficiency, used smaller networks. The hidden layer sizes were (84) and (84, 42, 21) for exergy destruction and exergy efficiency, compared to the hidden layer sizes for other models, (84, 84, 84) and (84, 84, 84, 84), which are significantly higher. This may indicate that the HPC models were simpler to regress [84,93]. Still, it should be noted that the hidden layer values have tended towards the upper range of the possible hyperparameter values, indicating a relatively complex regression problem.

The regularization hyperparameter value is also the highest possible across all models, indicating that some of the inputs used initially had a larger influence on the output, which required lowering in order to achieve a precise model. It should be noted that this may not indicate an operating point by itself as an input, but one of the values (steam temperature, pressure or mass flow rate) that were measured in it. Additionally, it can be seen that across all models, regularization is kept high, the preferred solver is LBFGS and the activation function is ReLU in all cases. While these hyperparameters do not provide additional information about the problem complexity, they can be utilized in further research in order to lower the number of combinations in the GS algorithm and allow for faster training times.

7. Conclusions

From the presented results it can be concluded that the calculation of exergy destruction and exergy efficiency of a marine steam turbine and its cylinders can be performed using artificial intelligence methods, namely MLP. Through the analysis of the results it can be seen that, while the best results are still achieved when using all the operating points, good results can be achieved using only a subset with negligible loss in accuracy and precision when MLP is used for modeling.

By observing the hyperparameter values which defined the model architecture of the selected models it can be concluded that the best solutions used relatively complex architectures, pointing towards a high complexity of this problem. While it is possible that even more precise solutions could be found using even more complex architectures, as the results provided are within the satisfactory error range, a further increase of computational complexity is needless.

Furthermore, by selecting a subset of the inputs which achieves relatively high results in all six output measurements (exergy destruction and exergy efficiency for LPC, HPC and WT) it can be concluded that, through the application of an MLP model, the number of operating points which can be used to determine the outputs can be lowered. This means that the costs of measuring equipment can be significantly lowered when this method is utilized. This is especially apparent in the selected case of operating points used being 1, 4 and 7 considering that measuring points 1 and 7 are already equipped through the subsequent and prior equipment in the maritime environment that the turbine is placed in. While the selected points do not provide the best results within the tested operating point input combinations, they provide good results across the entire range of modeled outputs and allow for the lowest amount of measuring equipment to be utilized. It may be possible to find an input combination that provides an even better fit for the presented problem. However, it should be noted that this could only be done by performing an extensive search of all possible operating point combinations as inputs, which would significantly raise the computational complexity, when the presented methodology is applied. The increase in computational complexity, in combination with the fact that models obtained by selecting a subset of input combinations provide a high quality solution, means that such an approach is unnecessary for the presented problem.

Further research will be performed in the following direction:

- (1) To determine optimal turbine operating points for the measurement of steam temperature, pressure and mass flow rate. The goal will be to find three or four operating points of which the measurement results, along with MLP application, can be used for exergy analysis parameters prediction of the whole turbine and each cylinder at any load, with the lowest possible errors.
- (2) Extensive measurements during a long time period will allow determining performance degradation coefficients for the whole analyzed turbine and each of its cylinders. Implementation of such coefficients inside MPL structure will allow accurate and precise predicting of turbine exergy analysis parameters for the entire period of its operation.
- (3) Investigate if the same technique can be applied for other main marine steam turbines (especially for newer variants, which consist of three cylinders and steam reheating).

The final goal will be to reduce the number of measurements (and to reduce the number of measuring equipment) for new ships with steam propulsion. The main idea is to perform MLP neural network training and testing on the manufacturer's test data at various loads along with the implementation of performance degradation coefficients inside the MLP structure. Such an approach will allow that onboard the ship, measurements of steam temperature, pressure and mass flow rate can be performed only in three or four optimal operating points (not in seven operating points as at the moment). By using the measurement results from a reduced number of operating points, the MLP neural network will be used for predicting the main steam turbine (and each cylinder) exergy destruction and exergy efficiency. In the end, the application of performance degradation coefficients will allow accurate and precise prediction of the whole turbine and its cylinders exergy analysis parameters for the entire steam power plant operation period.

If possible, the same idea presented in this paper for the main marine steam turbine and its cylinders will be applied to the entire marine steam propulsion plant.

Author Contributions: Conceptualization, S.B.Š., I.L., N.A., V.M. and Z.C.; methodology, V.M., I.L. and S.B.Š.; software, S.B.Š., N.A. and Z.C.; validation, I.L. and V.M.; formal analysis, N.A.; investigation, V.M., I.L., S.B.Š. and N.A.; resources, Z.C.; data curation, V.M.; writing—original draft preparation, V.M., I.L. and S.B.Š.; writing—review and editing, V.M., I.L., N.A. and S.B.Š.; visualization, I.L.; supervision, Z.C. and V.M.; project administration, Z.C.; funding acquisition, V.M. and Z.C. All authors have read and agreed to the published version of the manuscript.

Funding: This research has been supported by the Croatian Science Foundation under the project IP-2018-01-3739, CEEPUS network CIII-HR-0108, European Regional Development Fund under the grant KK.01.1.1.01.0009 (DATACROSS), project CEKOM under the grant KK.01.2.2.03.0004, CEI project “COVIDAi” (305.6019-20), University of Rijeka scientific grant uniri-tehnic-18-275-1447 and University of Rijeka scientific grant uniri-tehnic-18-18-1146.

Conflicts of Interest: The authors declare no conflict of interest.

Appendix A Specification of Used Measuring Equipment

Table A1. Temperature Measurements.

→ Greisinger GTF 601-Pt100	
Measuring range:	−200 to +600 °C
Response time:	approximate 10 s
Standard:	1/3 DIN class B
Error ranges:	$\pm(0.10 + 0.00167 Temp. \text{ in } ^\circ C)$
→ Greisinger GTF 401-Pt100	
Measuring range:	−50 to +400 °C
Response time:	approximate 10 s
Standard:	DIN class B
Error ranges:	$\pm(0.30 + 0.00500 Temp. \text{ in } ^\circ C)$

Table A2. Pressure Measurements.

→ Yamatake JTG960A	
Measuring span:	0.7 to 14 MPa
Setting range:	−0.1 to 14 MPa
Working pressure range:	2.0 kPa to 14 MPa
Accuracy:	$\pm 0.15\%$ for $\psi \geq 2.1$ MPa $\pm (0.05 + 0.1 \cdot \frac{2.1}{\psi})\%$ for $\psi < 2.1$ MPa
→ Yamatake JTG940A	
Measuring span:	35 to 3500 kPa
Setting range:	−100 to 3500 kPa
Working pressure range:	2.0 kPa to 3500 kPa
Accuracy:	$\pm 0.1\%$ for $\psi \geq 0.14$ MPa $\pm (0.025 + 0.75 \cdot \frac{0.14}{\psi})\%$ for $\psi < 0.14$ MPa

ψ = upper and lower limit of the calibration range (for both pressure measuring devices).

Table A3. Mass Flow Rate Measurements.

→ Yamatake JTG960A	
Measuring span:	0.25 to 14 MPa
Setting span:	−100 to 14 MPa
Working pressure range:	2.0 kPa to 14 MPa
Accuracy:	$\pm 0.15\%$ for $\psi \geq 3.5$ MPa $\pm (0.1 + 0.05 \cdot \frac{3.5}{\psi})\%$ for $\psi < 3.5$ MPa
→ Yamatake JTD930A	
Measuring span:	35 to 700 kPa
Setting span:	−100 to 700 kPa
Working pressure range:	2.0 kPa to 14 MPa
Accuracy:	$\pm 0.1\%$ for $\psi \geq 140$ kPa $\pm (0.025 + 0.075 \cdot \frac{140}{\psi})\%$ for $\psi < 140$ kPa
→ Yamatake JTD920A	
Measuring span:	0.75 to 100 kPa
Setting span:	−100 to 100 kPa
Working pressure range:	2.0 kPa to 14 MPa
Accuracy:	$\pm 0.1\%$ for $\psi \geq 5.0$ kPa $\pm (0.025 + 0.075 \cdot \frac{5.0}{\psi})\%$ for $\psi < 5.0$ kPa
→ Yamatake JTD910A	
Measuring span:	0.1 to 2 kPa
Setting span:	−1 to 1 kPa
Working pressure range:	up to 210 kPa
Accuracy:	$\pm (0.15 + 0.15 \cdot \frac{1.0}{\psi})\%$

ψ = upper and lower limit of the calibration range (for all mass flow rate measuring devices).

References

1. Tontu, M.; Sahin, B.; Bilgili, M. An exergoeconomic–environmental analysis of an organic Rankine cycle system integrated with a 660 MW steam power plant in terms of waste heat power generation. *Energy Sources Part A Recovery Util. Environ. Eff.* **2020**, *2020*, 1–22. [\[CrossRef\]](#)
2. Elhelw, M.; Al Dahma, K.S. Utilizing exergy analysis in studying the performance of steam power plant at two different operation mode. *Appl. Therm. Eng.* **2019**, *150*, 285–293. [\[CrossRef\]](#)

3. Uysal, C.; Kurt, H.; Kwak, H.Y. Exergetic and thermoeconomic analyses of a coal-fired power plant. *Int. J. Ther. Sci.* **2017**, *117*, 106–120. [\[CrossRef\]](#)
4. Naserbegi, A.; Aghaie, M.; Minuchehr, A.; Alahyarizadeh, G. A novel exergy optimization of Bushehr nuclear power plant by gravitational search algorithm (GSA). *Energy* **2018**, *148*, 373–385. [\[CrossRef\]](#)
5. Wilding, P.R.; Murray, N.R.; Memmott, M.J. The use of multi-objective optimization to improve the design process of nuclear power plant systems. *Ann. Nucl. Energy* **2020**, *137*, 107079. [\[CrossRef\]](#)
6. Adibhatla, S.; Kaushik, S.C. Exergy and thermoeconomic analyses of 500 MWe sub critical thermal power plant with solar aided feed water heating. *Appl. Therm. Eng.* **2017**, *123*, 340–352. [\[CrossRef\]](#)
7. Mehrpooya, M.; Ghorbani, B.; Sadeghzadeh, M. Hybrid solar parabolic dish power plant and high-temperature phase change material energy storage system. *Int. J. Energy Res.* **2019**, *43*, 5405–5420. [\[CrossRef\]](#)
8. Idris, M.N.M.; Hashim, H.; Razak, N.H. Spatial optimisation of oil palm biomass co-firing for emissions reduction in coal-fired power plant. *J. Clean. Prod.* **2018**, *172*, 3428–3447. [\[CrossRef\]](#)
9. Kim, D.; Kim, K.T.; Park, Y.K. A Comparative Study on the Reduction Effect in Greenhouse Gas Emissions between the Combined Heat and Power Plant and Boiler. *Sustainability* **2020**, *12*, 5144. [\[CrossRef\]](#)
10. Li, X.; Teng, Y.; Zhang, K.; Peng, H.; Cheng, F.; Yoshikawa, K. Mercury Migration Behavior from Flue Gas to Fly Ashes in a Commercial Coal-Fired CFB Power Plant. *Energies* **2020**, *13*, 1040. [\[CrossRef\]](#)
11. Nazir, S.M.; Bolland, O.; Amini, S. Analysis of combined cycle power plants with chemical looping reforming of natural gas and pre-combustion CO₂ capture. *Energies* **2018**, *11*, 147. [\[CrossRef\]](#)
12. Javadi, M.A.; Hoseinzadeh, S.; Ghasemiasl, R.; Heyns, P.S.; Chamkha, A.J. Sensitivity analysis of combined cycle parameters on exergy, economic, and environmental of a power plant. *J. Ther. Anal. Calor.* **2020**, *139*, 519–525. [\[CrossRef\]](#)
13. Rao, A.G.; Van den Oudenalder, F.S.C.; Klein, S.A. Natural gas displacement by wind curtailment utilization in combined-cycle power plants. *Energy* **2019**, *168*, 477–491. [\[CrossRef\]](#)
14. Kotowicz, J.; Brzęczek, M. Analysis of increasing efficiency of modern combined cycle power plant: A case study. *Energy* **2018**, *153*, 90–99. [\[CrossRef\]](#)
15. Pattanayak, L.; Sahu, J.N.; Mohanty, P. Combined cycle power plant performance evaluation using exergy and energy analysis. *Env. Progr. Sust. Energy* **2017**, *36*, 1180–1186. [\[CrossRef\]](#)
16. Okubo, M.; Kuwahara, T. *New Technologies for Emission Control in Marine Diesel Engines*; Butterworth-Heinemann: Oxford, UK, 2020.
17. Sartomo, A.; Santoso, B.; Muraza, O. Recent progress on mixing technology for water-emulsion fuel: A review. *Energy Convers. Manag.* **2020**, *213*, 112817. [\[CrossRef\]](#)
18. Senčić, T.; Mrzljak, V.; Blecich, P.; Bonefačić, I. 2D CFD simulation of water injection strategies in a large marine engine. *J. Mar. Sci. Eng.* **2019**, *7*, 296. [\[CrossRef\]](#)
19. Lamas Galdo, M.I.; Castro-Santos, L.; Rodriguez Vidal, C.G. Numerical analysis of NO_x reduction using ammonia injection and comparison with water injection. *J. Mar. Sci. Eng.* **2020**, *8*, 109. [\[CrossRef\]](#)
20. Fernández, I.A.; Gómez, M.R.; Gómez, J.R.; Insua, Á.B. Review of propulsion systems on LNG carriers. *Renew. Sustain. Energy Rev.* **2017**, *67*, 1395–1411. [\[CrossRef\]](#)
21. Ammar, N.R. Environmental and cost-effectiveness comparison of dual fuel propulsion options for emissions reduction onboard LNG carriers. *Shipbuilding* **2019**, *70*, 61–77. [\[CrossRef\]](#)
22. Altosole, M.; Benvenuto, G.; Zaccone, R.; Campora, U. Comparison of Saturated and Superheated Steam Plants for Waste-Heat Recovery of Dual-Fuel Marine Engines. *Energies* **2020**, *13*, 985. [\[CrossRef\]](#)
23. Altosole, M.; Benvenuto, G.; Campora, U.; Laviola, M.; Trucco, A. Waste heat recovery from marine gas turbines and diesel engines. *Energies* **2017**, *10*, 718. [\[CrossRef\]](#)
24. Grzesiak, S.; Adamkiewicz, A. Application of Steam Jet Injector for Latent Heat Recovery of Marine steam Turbine Propulsion Plant. *New Trend. Prod. Eng.* **2018**, *1*, 235–244. [\[CrossRef\]](#)
25. Marques, C.H.; Caprace, J.D.; Belchior, C.R.; Martini, A. An Approach for Predicting the Specific Fuel Consumption of Dual-Fuel Two-Stroke Marine Engines. *J. Mar. Sci. Eng.* **2019**, *7*, 20. [\[CrossRef\]](#)
26. Mrzljak, V.; Poljak, I.; Mrakovčić, T. Energy and exergy analysis of the turbo-generators and steam turbine for the main feed water pump drive on LNG carrier. *Energy Convers. Manag.* **2017**, *140*, 307–323. [\[CrossRef\]](#)
27. Behrendt, C.; Stoyanov, R. Operational characteristic of selected marine turbounits powered by steam from auxiliary oil-fired boilers. *New Trend. Prod. Eng.* **2018**, *1*, 495–501. [\[CrossRef\]](#)
28. Mrzljak, V. Low power steam turbine energy efficiency and losses during the developed power variation. *Tech. J.* **2018**, *12*, 174–180. [\[CrossRef\]](#)

29. Tanuma, T. *Advances in Steam Turbines for Modern Power Plants*; Woodhead Publishing: Cambridge, MA, USA, 2017.
30. Sun, L.; Hua, Q.; Shen, J.; Xue, Y.; Li, D.; Lee, K.Y. Multi-objective optimization for advanced superheater steam temperature control in a 300 MW power plant. *Appl. Energy* **2017**, *208*, 592–606. [\[CrossRef\]](#)
31. Szargut, J. *Exergy Method—Technical and Ecological Applications*; WIT Press: Southampton, UK, 2005.
32. Kanoglu, M.; Çengel, Y.A.; Dincer, I. *Efficiency Evaluation of Energy Systems*; Springer Briefs in Energy; Springer: Berlin/Heidelberg, Germany, 2012.
33. Ahmadi, G.R.; Toghraie, D. Energy and exergy analysis of Montazeri Steam Power Plant in Iran. *Renew Sustain. Energy Rev.* **2016**, *56*, 454–463. [\[CrossRef\]](#)
34. Si, N.; Zhao, Z.; Su, S.; Han, P.; Sun, Z.; Xu, J.; Cui, X.; Hu, S.; Wang, Y.; Jiang, L.; et al. Exergy analysis of a 1000 MW double reheat ultra-supercritical power plant. *Energy Convers. Manag.* **2017**, *147*, 155–165. [\[CrossRef\]](#)
35. Ibrahim, T.K.; Basrawi, F.; Awad, O.I.; Abdullah, A.N.; Najafi, G.; Mamat, R.; Hagos, F.Y. Thermal performance of gas turbine power plant based on exergy analysis. *Appl. Therm. Eng.* **2017**, *115*, 977–985. [\[CrossRef\]](#)
36. Aghbashlo, M.; Tabatabaei, M.; Hosseini, S.S.; Dashti, B.B.; Soufiyan, M.M. Performance assessment of a wind power plant using standard exergy and extended exergy accounting (EEA) approaches. *J. Clean. Prod.* **2018**, *171*, 127–136. [\[CrossRef\]](#)
37. AlZahrani, A.A.; Dincer, I. Energy and exergy analyses of a parabolic trough solar power plant using carbon dioxide power cycle. *Energy Convers. Manag.* **2018**, *158*, 476–488. [\[CrossRef\]](#)
38. Abuelnuor, A.A.A.; Saqr, K.M.; Mohieldin, S.A.A.; Dafallah, K.A.; Abdullah, M.M.; Nogoud, Y.A.M. Exergy analysis of Garri “2” 180 MW combined cycle power plant. *Renew. Sustain. Energy Rev.* **2017**, *79*, 960–969. [\[CrossRef\]](#)
39. Zhao, Z.; Su, S.; Si, N.; Hu, S.; Wang, Y.; Xu, J.; Jiang, L.; Chen, G.; Xiang, J. Exergy analysis of the turbine system in a 1000 MW double reheat ultra-supercritical power plant. *Energy* **2017**, *119*, 540–548. [\[CrossRef\]](#)
40. Medica-Viola, V.; Mrzljak, V.; Anđelić, N.; Jelić, M. Analysis of Low-Power Steam Turbine with One Extraction for Marine Applications. *Our Sea* **2020**, *67*, 87–95. [\[CrossRef\]](#)
41. Presciutti, A.; Asdrubali, F.; Baldinelli, G.; Rotili, A.; Malavasi, M.; Di Salvia, G. Energy and exergy analysis of glycerol combustion in an innovative flameless power plant. *J. Clean. Prod.* **2018**, *172*, 3817–3824. [\[CrossRef\]](#)
42. Szablowski, L.; Krawczyk, P.; Badyda, K.; Karellas, S.; Kakaras, E.; Bujalski, W. Energy and exergy analysis of adiabatic compressed air energy storage system. *Energy* **2017**, *138*, 12–18. [\[CrossRef\]](#)
43. Arshad, A.; Ali, H.M.; Habib, A.; Bashir, M.A.; Jabbal, M.; Yan, Y. Energy and exergy analysis of fuel cells: A review. *Therm. Sci. Eng. Progr.* **2019**, *9*, 308–321. [\[CrossRef\]](#)
44. Lorencin, I.; Anđelić, N.; Mrzljak, V.; Car, Z. Exergy analysis of marine steam turbine labyrinth (gland) seals. *Sci. J. Mar. Res.* **2019**, *33*, 76–83. [\[CrossRef\]](#)
45. Kavian, S.; Aghanajafi, C.; Mosleh, H.J.; Nazari, A.; Nazari, A. Exergy, economic and environmental evaluation of an optimized hybrid photovoltaic-geothermal heat pump system. *Appl. Energy* **2020**, *276*, 115469. [\[CrossRef\]](#)
46. Nami, H.; Anvari-Moghaddam, A. Geothermal driven micro-CCHP for domestic application—Exergy, economic and sustainability analysis. *Energy* **2020**, *207*, 118195. [\[CrossRef\]](#)
47. Liu, X.; Yang, X.; Yu, M.; Zhang, W.; Wang, Y.; Cui, P.; Zhu, Z.; Ma, Y.; Gao, J. Energy, exergy, economic and environmental (4E) analysis of an integrated process combining CO₂ capture and storage, an organic Rankine cycle and an absorption refrigeration cycle. *Energy Convers. Manag.* **2020**, *210*, 112738. [\[CrossRef\]](#)
48. Sun, K.; Wu, X.; Xue, J.; Ma, F. Development of a new multi-layer perceptron based soft sensor for SO₂ emissions in power plant. *J. Proc. Control* **2019**, *84*, 182–191. [\[CrossRef\]](#)
49. Hamed, W.; Salim, N. Use Data Mining Techniques to Identify Parameters That Influence Generated Power in Thermal Power Plant. *J ECS* **2017**, *17*, 52–64. Available online: <http://journal.sustech.edu/index.php/JECS/article/view/165> (accessed on 7 October 2020).
50. Lorencin, I.; Anđelić, N.; Mrzljak, V.; Car, Z. Genetic algorithm approach to design of multi-layer perceptron for combined cycle power plant electrical power output estimation. *Energies* **2019**, *12*, 4352. [\[CrossRef\]](#)
51. Khademi, M.; Moadel, M.; Khosravi, A. Power prediction and technoeconomic analysis of a solar PV power plant by MLP-ABC and COMFAR III, considering cloudy weather conditions. *Int. J. Chem. Eng.* **2016**, *2016*, 1031943. [\[CrossRef\]](#)
52. Demirdelen, T.; Aksu, I.O.; Esenboga, B.; Aygul, K.; Ekinci, F.; Bilgili, M. *A New Method for Generating Short-Term Power Forecasting Based on Artificial Neural Networks and Optimization Methods for Solar Photovoltaic Power Plants*; Springer Nature Singapore Pte Ltd.: Singapore, 2019. [\[CrossRef\]](#)

53. Wahid, F.; Ghazali, R.; Shah, A.S.; Fayaz, M. Prediction of energy consumption in the buildings using multi-layer perceptron and random forest. *IJAST* **2017**, *101*, 13–22. [\[CrossRef\]](#)
54. Tahan, M.; Tsoutsanis, E.; Muhammad, M.; Karim, Z.A. Performance-based health monitoring, diagnostics and prognostics for condition-based maintenance of gas turbines: A review. *Appl. Energy* **2017**, *198*, 122–144. [\[CrossRef\]](#)
55. Lorencin, I.; Anđelić, N.; Mrzljak, V.; Car, Z. Multilayer perceptron approach to condition-based maintenance of marine CODLAG propulsion system components. *Sci. J. Mar. Res.* **2019**, *33*, 181–190. [\[CrossRef\]](#)
56. Ferrero Bermejo, J.; Gómez Fernández, J.F.; Pino, R.; Crespo Márquez, A.; Guillén López, A.J. Review and Comparison of Intelligent Optimization Modelling Techniques for Energy Forecasting and Condition-Based Maintenance in PV Plants. *Energies* **2019**, *12*, 4163. [\[CrossRef\]](#)
57. Dixit, S.; Verma, N.K. Intelligent Condition Based Monitoring of Rotary Machines with Few Samples. *IEEE Sens. J.* **2020**, *2020*. [\[CrossRef\]](#)
58. Baressi Šegota, S.; Lorencin, I.; Musulin, J.; Štifanić, D.; Car, Z. Frigate Speed Estimation Using CODLAG Propulsion System Parameters and Multilayer Perceptron. *Our Sea* **2020**, *67*, 117–125. [\[CrossRef\]](#)
59. Dhini, A.; Kusumoputro, B.; Surjandari, I. Neural network based system for detecting and diagnosing faults in steam turbine of thermal power plant. In Proceedings of the 2017 IEEE 8th International Conference on Awareness Science and Technology (iCAST), Taichung, Taiwan, China, 8–10 November 2017; pp. 149–154. [\[CrossRef\]](#)
60. Tian, D.; Deng, J.; Vinod, G.; Santhosh, T.V.; Tawfik, H. A Neural Networks Design Methodology for Detecting Loss of Coolant Accidents in Nuclear Power Plants. In *Applications of Big Data Analytics*; Springer: Cham, Switzerland, 2018; pp. 43–61. [\[CrossRef\]](#)
61. Ayo-Imoru, R.M.; Cilliers, A.C. Continuous machine learning for abnormality identification to aid condition-based maintenance in nuclear power plant. *Ann. Nucl. Energy* **2018**, *118*, 61–70. [\[CrossRef\]](#)
62. Strušnik, D.; Avsec, J. Artificial neural networking and fuzzy logic exergy controlling model of combined heat and power system in thermal power plant. *Energy* **2015**, *80*, 318–330. [\[CrossRef\]](#)
63. Strušnik, D.; Golob, M.; Avsec, J. Artificial neural networking model for the prediction of high efficiency boiler steam generation and distribution. *Simul. Model. Pract. Theory* **2015**, *57*, 58–70. [\[CrossRef\]](#)
64. Agrež, M.; Avsec, J.; Strušnik, D. Entropy and exergy analysis of steam passing through an inlet steam turbine control valve assembly using artificial neural networks. *Int. J. Heat Mass Transf.* **2020**, *156*, 119897. [\[CrossRef\]](#)
65. *Marine Steam Turbine MS40-2—Instruction Book for Marine Turbine Unit*; Hyundai-Mitsubishi, Hyundai Heavy Industries, Co., Ltd.: Ulsan, Korea, 2004.
66. Mrzljak, V.; Poljak, I.; Medica-Viola, V. Dual fuel consumption and efficiency of marine steam generators for the propulsion of LNG carrier. *Appl. Therm. Eng.* **2017**, *119*, 331–346. [\[CrossRef\]](#)
67. Koroglu, T.; Sogut, O.S. Conventional and advanced exergy analyses of a marine steam power plant. *Energy* **2018**, *163*, 392–403. [\[CrossRef\]](#)
68. Çiçek, A.N. Exergy Analysis of a Crude Oil Carrier Steam Plant. Master's Thesis, Istanbul Technical University, Istanbul, Turkey, 2009. (In Turkish)
69. Mrzljak, V.; Poljak, I.; Medica-Viola, V. Thermodynamical analysis of high-pressure feed water heater in steam propulsion system during exploitation. *Shipbuilding* **2017**, *68*, 45–61. [\[CrossRef\]](#)
70. Taylor, D.A. *Introduction to Marine Engineering*, 2nd ed.; Elsevier Butterworth-Heinemann: Oxford, UK, 1996.
71. Škopac, L.; Medica-Viola, V.; Mrzljak, V. Selection Maps of Explicit Colebrook Approximations according to Calculation Time and Precision. *Heat Transf. Eng.* **2020**, *2020*, 1–15. [\[CrossRef\]](#)
72. Carlton, J. *Marine Propellers and Propulsion*, 4th ed.; Butterworth-Heinemann: Oxford, UK, 2019.
73. Kocijel, L.; Poljak, I.; Mrzljak, V.; Car, Z. Energy Loss Analysis at the Gland Seals of a Marine Turbo-Generator Steam Turbine. *Tech. J.* **2020**, *14*, 19–26. [\[CrossRef\]](#)
74. Moran, M.; Shapiro, H.; Boettner, D.D.; Bailey, M.B. *Fundamentals of Engineering Thermodynamics*, 7th ed.; John Wiley and Sons, Inc.: Hoboken, NJ, USA, 2011.
75. Fernández, I.A.; Gómez, M.R.; Gómez, J.R.; López-González, L.M. H₂ production by the steam reforming of excess boil off gas on LNG vessels. *Energy Convers Manag.* **2017**, *134*, 301–313. [\[CrossRef\]](#)
76. Medica-Viola, V.; Baressi Šegota, S.; Mrzljak, V.; Štifanić, D. Comparison of conventional and heat balance based energy analyses of steam turbine. *Sci. J. Mar. Res.* **2020**, *34*, 74–85. [\[CrossRef\]](#)
77. Dincer, I.; Rosen, M.A. *Exergy: Energy, Environment and Sustainable Development*, 2nd ed.; Elsevier: Oxford, UK, 2013.

78. Baldi, F.; Ahlgren, F.; Nguyen, T.V.; Thern, M.; Andersson, K. Energy and exergy analysis of a cruise ship. *Energies* **2018**, *11*, 2508. [\[CrossRef\]](#)
79. Kumar, V.; Pandya, B.; Matawala, V. Thermodynamic studies and parametric effects on exergetic performance of a steam power plant. *Int. J. Ambient. Energy* **2019**, *40*, 1–11. [\[CrossRef\]](#)
80. Mrzljak, V.; Blecich, P.; Anđelić, N.; Lorencin, I. Energy and exergy analyses of forced draft fan for marine steam propulsion system during load change. *J. Mar. Sci. Eng.* **2019**, *7*, 381. [\[CrossRef\]](#)
81. Ray, T.K.; Datta, A.; Gupta, A.; Ganguly, R. Exergy-based performance analysis for proper O&M decisions in a steam power plant. *Energy Convers. Manag.* **2010**, *51*, 1333–1344. [\[CrossRef\]](#)
82. Aljundi, I.H. Energy and exergy analysis of a steam power plant in Jordan. *Appl. Therm. Eng.* **2009**, *29*, 324–328. [\[CrossRef\]](#)
83. Mrzljak, V.; Senčić, T.; Žarković, B. Turbogenerator Steam Turbine Variation in Developed Power: Analysis of Exergy Efficiency and Exergy Destruction Change. *Model. Simul. Eng.* **2018**, *2018*, 2945325. [\[CrossRef\]](#)
84. Tan, H.; Shan, S.; Nie, Y.; Zhao, Q. A new boil-off gas re-liquefaction system for LNG carriers based on dual mixed refrigerant cycle. *Cryogenics* **2018**, *92*, 84–92. [\[CrossRef\]](#)
85. Noroozian, A.; Mohammadi, A.; Bidi, M.; Ahmadi, M.H. Energy, exergy and economic analyses of a novel system to recover waste heat and water in steam power plants. *Energy Convers. Manag.* **2017**, *144*, 351–360. [\[CrossRef\]](#)
86. Nanaki, E.A.; Xydis, G. *Exergetic Aspects of Renewable Energy Systems: Insights to Transportation and Energy Sector for Intelligent Communities*; CRC Press: Boca Raton, FL, USA, 2019.
87. Erdem, H.H.; Akkaya, A.V.; Cetin, B.; Dagdas, A.; Sevilgen, S.H.; Sahin, B.; Teke, I.; Gungor, C.; Atas, S. Comparative energetic and exergetic performance analyses for coal-fired thermal power plants in Turkey. *Int. J. Therm. Sci.* **2009**, *48*, 2179–2186. [\[CrossRef\]](#)
88. Adibhatla, S.; Kaushik, S.C. Energy and exergy analysis of a super critical thermal power plant at various load conditions under constant and pure sliding pressure operation. *Appl. Therm. Eng.* **2014**, *73*, 51–65. [\[CrossRef\]](#)
89. Goodfellow, I.; Bengio, Y.; Courville, A. *Deep Learning*; The MIT Press: Cambridge, MA, USA, 2016.
90. Moon, T.; Hong, S.; Choi, H.Y.; Jung, D.H.; Chang, S.H.; Son, J.E. Interpolation of greenhouse environment data using multilayer perceptron. *Comput. Electron. Agric.* **2019**, *166*, 105023. [\[CrossRef\]](#)
91. Lorencin, I.; Anđelić, N.; Španjol, J.; Car, Z. Using multi-layer perceptron with Laplacian edge detector for bladder cancer diagnosis. *Artif. Intell. Med.* **2020**, *102*, 101746. [\[CrossRef\]](#)
92. Car, Z.; Baressi Šegota, S.; Anđelić, N.; Lorencin, I.; Mrzljak, V. Modeling the Spread of COVID-19 Infection Using a Multilayer Perceptron. *Comput. Math. Methods Med.* **2020**, *2020*, 5714714. [\[CrossRef\]](#) [\[PubMed\]](#)
93. Khalid, A.; Sundararajan, A.; Acharya, I.; Sarwat, A.I. Prediction of li-ion battery state of charge using multilayer perceptron and long short-term memory models. In Proceedings of the 2019 IEEE Transportation Electrification Conference and Expo (ITEC), Detroit, MI, USA, 19–21 June 2019; pp. 1–6. [\[CrossRef\]](#)
94. Bisong, E. *The Multilayer Perceptron (MLP). Building Machine Learning and Deep Learning Models on Google Cloud Platform*; Apress: Berkeley, CA, USA, 2019; pp. 401–405. [\[CrossRef\]](#)
95. Eger, S.; Youssef, P.; Gurevych, I. Is it time to swish? Comparing deep learning activation functions across NLP tasks. *arXiv* **2019**, arXiv:1901.02671.
96. Jagtap, A.D.; Kawaguchi, K.; Karniadakis, G.E. Locally adaptive activation functions with slope recovery term for deep and physics-informed neural networks. *Proc. R. Soc. A* **2020**, *476*, 20200334. [\[CrossRef\]](#)
97. Dureja, A.; Pahwa, P. Analysis of non-linear activation functions for classification tasks using convolutional neural networks. *Recent Pat. Comput. Sci.* **2019**, *12*, 156–161. [\[CrossRef\]](#)
98. Hastie, T.; Tibshirani, R.; Friedman, J. *The Elements of Statistical Learning: Data Mining, Inference, and Prediction*, 2nd ed.; Springer Science & Business Media: New York, NY, USA, 2009.
99. Pedregosa, F.; Varoquaux, G.; Gramfort, A.; Michel, V.; Thirion, B.; Grisel, O.; Blondel, M.; Prettenhofer, P.; Weiss, R.; Dubourg, V.; et al. Scikit-learn: Machine learning in Python. *J. Mach. Learn. Res.* **2011**, *12*, 2825–2830.
100. Abraham, A.; Pedregosa, F.; Eickenberg, M.; Gervais, P.; Mueller, A.; Kossaifi, J.; Gramfort, A.; Thirion, B.; Varoquaux, G. Machine learning for neuroimaging with scikit-learn. *Front. Neuroinf* **2014**, *8*, 14. [\[CrossRef\]](#)
101. Géron, A. *Hands-On Machine Learning with Scikit-Learn, Keras, and TensorFlow: Concepts, Tools, and Techniques to Build Intelligent Systems*, 2nd ed.; O'Reilly Media: Sebastopol, CA, USA, 2019.

102. Liashchynskiy, P.; Liashchynskiy, P. Grid Search, Random Search, Genetic Algorithm: A Big Comparison for NAS. *arXiv* **2019**, arXiv:1912.06059.
103. Bari, A.H.; Gavrilova, M.L. Multi-layer perceptron architecture for kinect-based gait recognition. In Proceedings of the Computer Graphics International Conference, Calgary, AB, Canada, 17–20 June 2019; Springer: Cham, Switzerland; pp. 356–363. [\[CrossRef\]](#)
104. Sakar, C.O.; Polat, S.O.; Katircioglu, M.; Kastro, Y. Real-time prediction of online shoppers' purchasing intention using multilayer perceptron and LSTM recurrent neural networks. *Neural Comput. Appl.* **2019**, *31*, 6893–6908. [\[CrossRef\]](#)
105. Nagelkerke, N.J. A note on a general definition of the coefficient of determination. *Biometrika* **1991**, *78*, 691–692. [\[CrossRef\]](#)
106. Nakagawa, S.; Johnson, P.C.; Schielzeth, H. The coefficient of determination R^2 and intra-class correlation coefficient from generalized linear mixed-effects models revisited and expanded. *J. R. Soc. Interface* **2017**, *14*, 20170213. [\[CrossRef\]](#)
107. Qi, J.; Du, J.; Siniscalchi, S.M.; Ma, X.; Lee, C.H. On mean absolute error for deep neural network based vector-to-vector regression. *IEEE Signal Proc. Lett.* **2020**, *27*, 1485–1489. [\[CrossRef\]](#)
108. Štifanić, D.; Musulin, J.; Miočević, A.; Baressi Šegota, S.; Šubić, R.; Car, Z. Impact of COVID-19 on Forecasting Stock Prices: An Integration of Stationary Wavelet Transform and Bidirectional Long Short-Term Memory. *Complexity* **2020**, *2020*, 1846926. [\[CrossRef\]](#)
109. Berrar, D. Cross-validation. *Encycl. Bioinform. Comput. Biol.* **2019**, *1*, 542–545.
110. Bishop, C.M. *Pattern Recognition and Machine Learning*; Springer: New York, NY, USA, 2006.
111. Moayedi, H.; Osouli, A.; Nguyen, H.; Rashid, A.S.A. A novel Harris hawks' optimization and k-fold cross-validation predicting slope stability. *Eng. Comput.* **2019**, *2019*, 1–11. [\[CrossRef\]](#)
112. BURA Supercomputer, Computing Resources. Available online: <https://cnrm.uniri.hr/bura/> (accessed on 30 October 2020).
113. Anaconda Software Distribution. Anaconda Documentation. Anaconda Inc. 2020. Available online: <https://docs.anaconda.com/> (accessed on 30 October 2020).
114. Lemmon, E.W.; Huber, M.L.; McLinden, M.O. *Reference Fluid Thermodynamic and Transport Properties-REFPROP*; Version 9.0, User's Guide; NIST: Gaithersburg, MD, USA, 2010.
115. Mrzljak, V.; Poljak, I.; Žarković, B. Exergy analysis of steam pressure reduction valve in marine propulsion plant on conventional LNG carrier. *Our Sea* **2018**, *65*, 24–31. [\[CrossRef\]](#)
116. SUITABLE PT100 MEASURING PROBE (4-WIRE). Available online: https://www.greisinger.de/files/upload/en/produkte/kat/k16_011_EN_oP.pdf (accessed on 3 October 2020).
117. JTG Series of Pressure Transmitters. Available online: http://smte.kr/product/data/pdf/pdf_100812100836_552363.pdf (accessed on 4 October 2020).
118. JTD Series of Differential Pressure Transmitters. Available online: http://www.krtproduct.com/krt_Picture/sample/1_spare%20part/yamatake/Fi_ss01/SS2-DST100-0100.pdf (accessed on 3 October 2020).

Publisher's Note: MDPI stays neutral with regard to jurisdictional claims in published maps and institutional affiliations.



© 2020 by the authors. Licensee MDPI, Basel, Switzerland. This article is an open access article distributed under the terms and conditions of the Creative Commons Attribution (CC BY) license (<http://creativecommons.org/licenses/by/4.0/>).